On the efficiency of mitigation measures in reducing the amplified response at transition zones in railway tracks: tuned mass dampers, auxiliary rails, and under-sleeper pads

By

Behnam Jouna

Submitted to the Department of Engineering Structures in Partial Fulfillment of the Requirements for the Degree of

Master of Science in Structural Engineering
at
Delft University of Technology

Thesis Committee:
Dr. Karel van Dalen (Chair)
Prof. Andrei Metrikine
Ir. Andrei Fărăgău

TUDelft

به نام خداوند بخشنده مهربان

To my beloved mother and father

Abstract

In transition zones, railway tracks experience significant inhomogeneity in their mechanical properties—more specifically in vertical stiffness. In such areas, conventional tracks (soft tracks) are typically encountered with other engineering structures with noticeably larger stiffness, such as bridges and culverts (stiff tracks). This inhomogeneity together with the passage of high-speed trains leads to amplification in dynamic response, which in turn results in faster degradation and higher cost of maintenance at transition zones. In practice, various mitigation measures have been adopted which have led to improvement in track performance to a certain degree.

This thesis is mainly focused on the feasibility of using the tuned mass damper (TMD), as a novel mitigation measure, for improving the aforementioned undesired behavior. Additionally, the efficiency of two already existing corrective measures, namely auxiliary rail and under sleeper pad (USP), is investigated at transition zone.

The track is modeled as an infinite one-dimensional Euler-Bernoulli beam resting on a piecewise-homogeneous and continuously distributed Kelvin foundation. For each mitigation measure, semi-analytical solutions are derived through the Fourier transform method. Regarding TMD analysis, mechanical parameters are optimized by an evolutionary algorithm (NSGA-II), in which the discrepancy between the soft and the stiff tracks' wavenumbers is minimized. In regard to auxiliary rail, two configurations with multiple number of extra rails (ERs) are evaluated; ERs over soft track only, and ERs over all domains. Additionally, USPs with different stiffness are considered for their arrangement along the track. The efficiency corresponding to each mitigation measure is mainly evaluated through dynamic amplification factor (DAF) and power input.

The system with TMD demonstrates a significant reduction in DAF amplitude corresponding to the load velocity for which the optimization is performed. This improvement is also evident for velocities close to the aforementioned load speed. In fact, the addition of TMD results in presence of a free propagating wave behind

the load and decreasing the critical velocity in the corresponding system. The outcomes corresponding to power input suggest a significant reduction in potential damage to the foundation due to the employment of TMD.

Furthermore, the application of ER leads to improvement in dynamic performance of the track by increasing the critical velocity to a larger value, at which the corresponding DAF indicates no reduction. In addition, considering more than one ER along the track does not lead to a noticeably better result compared to when only one ER is added. Moreover, applying ER over soft track leads to inhomogeneity in bending stiffness and mass corresponding to the beam element at transition point. Therefore, the system with ER over all domains indicates a better dynamic behavior. Potentially, less damage to the foundation can be signified in the system with ER according to the power input response.

Finally, USP can significantly affect the equivalent stiffness of the track. It is concluded that the efficiency of USPs in mitigating the amplified response is strongly dependent on their stiffness and arrangement along the track, as well as the stiffness variation in the supporting structure; improper design of USPs alignment can adversely result in even more amplified responses.

Contents

Appendices   59

A   59

Chapter 1

Introduction

1.1   Background

Railway networks play an important role in the efficiency of modern transportation systems. On an international scale, noticeable investments are annually considered for railway infrastructures corresponding to their maintenance and operations. In 2015, for example, more than half of the total budget of the Spanish infrastructures was dedicated to the railway networks only (Sañudo et al. 2016).

In practice, the maintenance works are performed more often in transition zones (Dahlberg 2010; Z. Li and Wu 2008; Seara and Correia 2010), the regions where the tracks experience structural discontinuities and therefore significant variations in their mechanical properties. This inhomogeneity together with the passage of high-speed trains results in faster degradation of the track geometry. Almost half of the transition zones indicate settlements in the form of dip (Stark and Wilk 2016) with the magnitude, in some cases, of about 5mm (Nicks 2009). This in turn increases the dynamic loads (José N Varandas et al. 2011) leading to further damages such as hanging sleepers, cracks in concrete sleepers and rail foot, etc.

Reportedly, the number of maintenance programs at transition zones is three to eight times more than the regular tracks (Sañudo et al. 2016; Wang and Markine 2018). Consequently, a major prominence has been received to this issue by researchers and concerning organizations to reduce the cost of maintenance and secure the operations of railway networks with the least disruption to traffic. Various mitigation measures, therefore, have been proposed and applied with some of them demonstrating improvement to a certain degree. Further studies, however, are still being carried out in achieving more efficient solutions.

1.2   Research motivation

To counteract the earlier mentioned issues at transition zones, particular features should be recognized either at the initial stages of designing a new track or at the rehabilitation level of the existing tracks. In-site operations corresponding to the latter might be extremely challenging and costly such that the traffic flow is required to be stopped. Additionally, not all counteractive measures are sufficiently effective while in a few cases, they can even adversely affect the track behavior at transition zone. Note that various methods can be considered when analyzing a design solution, namely mechanical and numerical modeling, field investigations, and off-site experimental tests.

The goal of this thesis is to identify promising mitigation measures and inves-

tigate their efficiencies in reduction of the amplified response at transition zones in railway tracks. While doing so, considering both novel and the already existing measures are of interest. The focus of the latter when identified, however, is more on the extension of the past evaluations. Then, it is aimed at investigating their effects on dynamic behavior at transition zone through analyzing the mechanical model of the train-track system.

1.3   Literature review

Despite extensive studies in the past, no definite reason can be attributed to the undesired behaviors in transition zones due to the inherent complexity of train-track systems. However, substantial variation in vertical stiffness along the track, low quality of geotechnical components, and differential settlements can be mentioned as some of the main factors (Sañudo et al. 2016; Stark and Wilk 2016; J. Varandas et al. 2017).

A review of various solutions evaluated by previous researchers can be found in (Indraratna et al. 2019; Sañudo et al. 2016). The mitigation measures mostly have been focused on smoothing the stiffness gradient in the transition zones, either by modifying the track's superstructure or substructure exclusively, or by rectifying both together. That is, increasing the stiffness of conventional tracks and reducing the stiffness of the tracks with/over rigid structures—such as bridges and tunnels.

The substructure's main function is to uniformly resist the train loads such that the track geometry is maintained. Soils can be reinforced by applying geosynthetic materials (increase load-bearing capacity) (Horníček et al. 2010), geocells (better load distribution), and cement gravels. Even though being an expensive solution, incorporating piles under the ballast can also reinforce the track foundation which leads to an increase in stiffness and a considerable reduction in the settlement. Moreover, the load-bearing capacity of the subgrade (but not the ballast) can be improved by a layer of hot mix asphalt over it. Integration of transition slabs into the track is another mitigation measure that requires the substructure to be modified. In an experimental work, (Fara 2014) suggests that transition slabs improve the track behavior until one year; nevertheless, afterward, the corresponding performance develops into even more degradation compared to the track before the modification.

At superstructure level, progressive enhancement of the sleepers' length toward the rigid structure, together with a gradual reduction in their bay spacing can increase the track stiffness. However, contribution of the achieved resiliency to

the ballast is not significant (NAMURA et al. 2004). The application of the
sleepers made up of less resilient materials (e.g. plastic and rubber) demonstrates
a reduction in the track stiffness (Sasaoka and Davis 2005). As another mitigation
measure, adjustable rail fasteners are employed to remove the gap under the hanger
sleepers; (Wang and Markine 2018) suggests that this solution significantly reduces
the ballast degradation rate and improves the stress distribution in the ballast.
Moreover, applying resin glue to the ballast results in a substantial decrease in
track settlement (Kennedy et al. 2013).

Employment of the auxiliary rail is another method to increase the resiliency
of the track. They improve the stress distribution in the ballast and dynamic
behavior in the transition areas (Chumyen et al. 2022). Note that in practice, the
installation of extra rails does not result in major disruption in traffic flow while
the track mainly remains intact. Despite these advantages, not many studies have
been focused on the efficiency of extra rails.

According to (Schneider et al. 2011), under sleeper pad (USP) increase the rail
and the sleeper accelerations. Nevertheless, the application of USP reduces the
degradation rate of the track geometry and can improve the stiffness variation.
The employment of USPs requires extra attention as its potential efficiency is
not guaranteed for any arrangement along the track. Therefore, studying the
corresponding alignment is of high importance.

Notice that the aim of smoothing the stiffness variation is eventually to reduce
the amplified vibrations. In the context of vibration control, tuned mass damper
(TMD) has been widely applied within various engineering fields; from controlling
vibrations in hair clippers to reducing the nature-induced vibrations in skyscrapers.
TMD is normally tuned to resonance frequency of the host structure to which it
is attached. When the aforementioned frequency is excited, the TMD absorbs the
structure vibrations through counteracting forces (out of phase motions) and its
dissipative element. To the best of the author's knowledge, the efficiency of TMD
in reducing the amplified response at transition zone has not been studied yet.

In line with previous paragraphs, three mitigation measures are therefore adopted
to be investigated herein; that is, tuned mass damper, auxiliary rail, and under
sleeper pad.

1.4   Research questions

The thesis objectives are formulated through the following research questions.

1. As a novel mitigation measure, to what extent is the application of TMD efficient in reducing the amplified vibrations at transition zone?

2. What arrangement of the extra rails does contribute the most to decreasing the undesired mechanical response in the transition area?

3. How does the arrangement of USPs affect the correspondent efficiency in mitigating the transition zone's behavior?

1.5 Outline

Throughout this document, three mitigation measures are considered with the TMD being the main focus of the thesis. For each solution, a chapter is dedicated starting with its corresponding literature review. In chapter 2, the applicability of TMD is studied, in which the train-track system is modeled as an infinite one-dimensional Euler-Bernoulli beam resting on a piece-wise homogeneous foundation. Semi-analytical solutions are then derived through the Fourier transform method while an evolutionary optimization is considered for tuning the design variables of TMD. Moreover, the results are evaluated in both frequency and time domains while the energy considerations are also addressed. Next, the aforementioned mechanical model is accordingly modified for the employment of auxiliary rail and USP in chapter 3 and chapter 4, respectively, in which their corresponding dynamic analyses and outcomes are naturally presented. Finally, in chapter 5, overall findings of the thesis are discussed and conclusions are established.

Chapter 2

Tuned Mass Damper

In this chapter, the efficiency of tuned mass damper, TMD, in reducing the amplified vibrations is investigated. Initially, a literature review corresponding to vibration control using TMD is presented. Next, a simplified mechanical model is established for the railway transition zone while the TMDs are incorporated into the system by distributing them along the track. Dynamic response of the system is then described by a set of partial differential equations. Afterward, solutions are derived through transforming the equations of motions to the Fourier domain over time which are numerically cast back into the space-time domain. To attenuate the undesired vibrations in transition zone, the TMD's mechanical parameters are tuned through a well known optimization algorithm, NSGA-II, such that the discrepancy in the wavenumbers of the soft and the stiff tracks is minimized. To investigate the efficiency of TMD, the systems are analyzed through dispersion relations, displacement fields, and energy considerations. It is concluded that TMDs can significantly improve the transition zone's behavior at load velocity for which they are optimized.

2.1   Literature review

The origin of TMD concept is attributed to the invention of a German engineer (Frahm 1911), in which vibrations are controlled without damping element. TMD is normally tuned to the resonance frequency of the main structure to which it is attached. When the tuned frequency is excited, the TMD suppresses the structure vibrations. The absence of damping component results in considerable sensitivity of TMD system to the off-tuned conditions, while its presence leads to addition of neighboring frequencies to the tuned frequency at which the vibration is absorbed (F. Yang et al. 2022). Generally, to achieve an effective design, the corresponding parameters need to be optimized. The first optimization analysis of TMD, in its classic form (consisting of mass, stiffness, and damping element), is associated to the work by (Den Hartog 1985).

Over the last decades, the application of TMD has been modified and extended to various engineering fields. State-of-the-art corresponding to TMD and vibration control can be found in (Elias and Matsagar 2017; F. Yang et al. 2022). Due to robust design, nearly inexpensive cost, resistance to high temperatures, and capability of large structural damping, the TMDs have been extensively applied for controlling the nature-induced vibrations (e.g. earthquakes and winds) in civil structures (F. Yang et al. 2022); C N Tower (Canada, 1973), Sydney Tower (Australia, 1980), Crystal Tower (Japan, 1990), and Taipei 101 Tower (Taiwan, 2004) can be mentioned as a few examples. This study concludes that single tuned mass

damper (STMD) is most efficient when tuned to fundamental mode of the primary structure. Moreover, the TMD with larger mass is normally more effective in suppressing the structural vibrations. However, due to physical limitations in practice, the employment of multiple tuned mass dampers (MTMD) has been proposed by researchers. In fact, dampers are distributed along the spatial domain of structures. Same study suggests that MTMD is more effective compared to STMD.

(Esmailzadeh and Jalili 1998) derived the coupled EOMs of a cantilever beam under an arbitrary distributed load where TMDs were applied to suppress the dynamic response over arbitrary number of resonance frequencies; the absorbers were optimized through Direct Updated Method. Furthermore, (Lin et al. 2005) modeled a railway bridge as a continuous Euler-Bernoulli beam under moving loads where MTMD were optimized for resonant speeds; this study concludes that MTMD technique is more effective in reducing the bridge dynamic response compared to the employment of STMD. In another study, (Hadi and Arfiadi 1998) optimized the TMDs via Genetic Algorithm for protecting building structures against seismic vibrations. Similarly, (Kaveh, Mohammadi, et al. 2015) performed an optimization for multistory structures but with a heuristic algorithm known as Charge System Search in (Kaveh and Talatahari 2010). As can be seen, various optimization methods have been adopted for tuning the vibration absorbers.

On the other hand, previous findings in railway engineering have been largely focused on noise radiation control when TMD is considered (it is commonly known as rail damper). Rail dampers are normally installed in the middle of the sleeper bay to suppress the noise radiation in the rail which is attributed to pined-pined vibrations between the sleepers (Xiao et al. 2017). The principle is therefore different from controlling the vibrations at transition zone.

2.2 Train-track system with TMD

2.2.1 Mechanical model

The track is modeled as an infinite one-dimensional Euler-Bernoulli beam resting on a continuously distributed Kelvin foundation along the longitudinal direction, x, as can be seen in Figure 2.1. The infinite track is divided into two semi-infinite homogeneous domains which are connected to each other at the interface/transition point, $x_{tp} = 0$. The left ($x \leqslant x_{tp}$) and the right ($x \geqslant x_{tp}$) domains are referred to the soft and the stiff tracks with subscript $j = 1$ and $j = 2$, respectively.
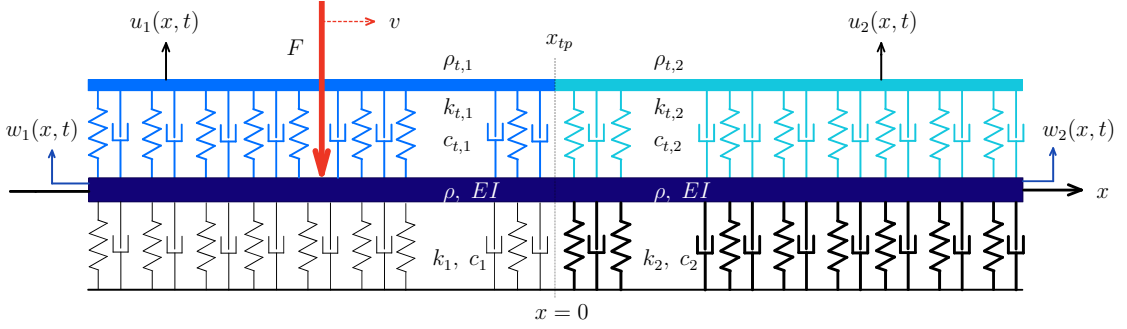
Figure 2.1: Scheme of the track mechanical model with TMDs.

The piecewise-homogeneous foundation accounts for the equivalent static stiffness and damping of the track excluding the rail (but including the rail fastening system, ballast, and substructure layers) which are indicated by k_j and c_j, respectively. Moreover, c_j is defined as $2\zeta\sqrt{k_j\,\rho_j}$ with ζ being the damping ratio—unrelated to the actual damping relative to the critical damping in the SDOF system (Fărăgău, Keijdener, et al. 2021). Furthermore, the train is modeled as a constant moving point-load with the magnitude of F. Starting from the left domain, it moves rightward[1] with the constant velocity, v.

Linear density of the beam element is denoted by ρ (per unit length). Important to note, in this simplified model, bending stiffness of the track components is limited to that of the Euler-Bernoulli beam, EI, only. In addition, no internal damping, rotational or longitudinal vibration is considered.

Furthermore, the TMDs are continuously distributed over the beam and along the longitudinal direction; $\rho_{t,j}$ demonstrate the TMDs linear mass while $k_{t,j}$ and $c_{t,j}$ describe the continuously distributed stiffness and dampings of the TMDs, respectively. In addition, the displacements corresponding to the beams and TMDs are respectively denoted by w_j and u_j, in which both are dependent on the space, x, and time, t.

2.2.2   Equations of motions

The equations of motions, EOMs, describing vertical vibrations are derived as

$$EIw_j^{''''} + \rho\ddot{w}_j + (c_j + c_{t,j})\dot{w}_j + (k_j + k_{t,j})w_j - c_{t,j}\dot{u}_j - k_{t,j}u_j = -F\delta(x - vt), \tag{2.1a}$$

$$\rho_{t,j}\ddot{u}_j + c_{t,j}\dot{u}_j + k_{t,j}u_j - c_{t,j}\dot{w}_j - k_{t,j}w_j = 0, \tag{2.1b}$$

---

[1]The vice versa movement is neglected in this study as the amplified responses are normally much more stronger for the rightward traveling from the soft track (Sañudo et al. 2016).

where $\delta(\cdot)$ is Dirac-Delta function specifying the position of moving load while the primes and overdots indicate $\frac{\partial}{\partial x}$ and $\frac{\partial}{\partial t}$, respectively.

The boundary conditions necessitate zero displacement at infinite distance from the moving load, due to damping in the system;

$$\lim_{(x-vt)\to-\infty} w_1(x,t) = 0, \tag{2.2a}$$

$$\lim_{(x-vt)\to+\infty} w_2(x,t) = 0. \tag{2.2b}$$

Moreover, the interface conditions provide continuity at transition point x_{tp}, which is correspondent to the beam displacement, slope $\phi(x,t) = -w'$, bending moment $M(x,t) = -EIw''(x,t)$, and shear force $V(x,t) = -EIw'''(x,t)$;

$$w_1(x_{tp},t) = w_2(x_{tp},t), \tag{2.3a}$$

$$w_1'(x_{tp},t) = w_2'(x_{tp},t), \tag{2.3b}$$

$$w_1''(x_{tp},t) = w_2''(x_{tp},t), \tag{2.3c}$$

$$w_1'''(x_{tp},t) = w_2'''(x_{tp},t). \tag{2.3d}$$

2.2.3 Semi-analytical solutions

To determine the response to the system described by Equation 2.1, the forward Fourier transform is applied over time;

$$\widetilde{w}_j(x,\omega) = \int_{-\infty}^{\infty} w_j(x,t)e^{-i\omega t}\mathrm{d}t, \tag{2.4a}$$

$$\tilde{u}_j(x,\omega) = \int_{-\infty}^{\infty} u_j(x,t)e^{-i\omega t}\mathrm{d}t, \tag{2.4b}$$

where ω is angular frequency (rad/s), and $i = \sqrt{-1}$ is imaginary unit.

Considering the property of Dirac delta function (Boas 2006),

$$\delta(g(s)) = \sum_m \frac{\delta(s-s_m)}{|g'(s_m)|} \quad \text{with } s_m \text{ being the roots of } g, \text{ and} \tag{2.5a}$$

$$\int_{-\infty}^{\infty} \delta(s-a)q(s)\mathrm{d}s = q(a), \tag{2.5b}$$

the right side of the Equation 2.1a reads

$$-\int_{-\infty}^{\infty} F\delta(x - vt)e^{-i\omega t}dt = -\int_{-\infty}^{\infty} \frac{F\delta(t - x/v)e^{-i\omega t}}{v}dt = -\frac{Fe^{-i\omega x/v}}{v}. \qquad (2.6a)$$

The EOMs in frequency domain is therefore obtained as

$$EI\widetilde{w}_j'''' + (-\rho\omega_j^2 + i(c_j + c_{t,j})\omega + k_j + k_{t,j})\widetilde{w}_j - (ic_{t,j}\omega + k_{t,j})\tilde{u}_j = -\frac{Fe^{-i\omega x/v}}{v}, \qquad (2.7a)$$

$$\tilde{u}_j = \frac{(ic_{t,j}\omega + k_{t,j})}{(-\rho_{t,j}\omega^2 + ic_{t,j}\omega + k_{t,j})}\widetilde{w}_j. \qquad (2.7b)$$

Substituting $\tilde{u}_j$ into the Equation 2.7a gives

$$\widetilde{w}_j'''' - \beta_j^4 \widetilde{w}_j = -\frac{Fe^{i\omega x/v}}{vEI}, \qquad (2.8a)$$

where β_j denote the wavenumbers, and

$$\beta_j^4 = (\rho\omega^2 - i\omega(c_j + c_{t,j}) - k_j - k_{t,j})/EI + \frac{(i\omega c_{t,j} + k_{t,j})^2}{(-\rho_{t,j}\omega^2 + ic_{t,j}\omega + k_{t,j})EI}. \qquad (2.9a)$$

By substituting the trial solutions in the form of $Ce^{-i\omega x/v}$ in Equation 2.8a and removing the common factors, particular solutions read

$$\widetilde{w}_{j,p}(x,\omega) = \frac{-Fv^3 e^{-i\omega x/v}}{EI(\omega^4 - \beta_j^4 v^4)}. \qquad (2.10a)$$

Furthermore, by substituting the trial solutions in the form of $Ae^{\lambda_1 x}$ and $Be^{\lambda_2 x}$, into the homogeneous form of Equation 2.8a and then removing the common factors, homogeneous solutions are derived as

$$\widetilde{w}_{1,h}(x,\omega) = \sum_{n=1}^{4} A_n e^{\lambda_{1,n} x}, \qquad x \leqslant x_{tp}, \qquad (2.11a)$$

$$\widetilde{w}_{2,h}(x,\omega) = \sum_{n=1}^{4} B_n e^{\lambda_{2,n} x}, \qquad x \geqslant x_{tp}, \qquad (2.11b)$$

in which the roots of characteristic equations ($\lambda_j^4 = \beta_j^4$) read

$$\lambda_{j,1} = \beta_j, \qquad \lambda_{j,2} = i\beta_j, \qquad \lambda_{j,3} = -\lambda_{j,1}, \qquad \lambda_{j,4} = -\lambda_{j,2}. \qquad (2.12a)$$

Four distinct roots (wavenumbers) corresponding to the Equation 2.9a can be derived through de Moivre's theorem in polar form as follows (Kreyszig 2010);

Let $z \neq 0$ be a complex number. The n distinct n^{th} roots of z are

$$\sqrt[n]{z} = \sqrt[n]{r} \left(\cos \left(\frac{\theta + 2k\pi}{n} \right) + i \sin \left(\frac{\theta + 2k\pi}{n} \right) \right), \qquad (2.13)$$

where

r is the modulus of z,
θ is the argument of z,
$k = 0, 1, \cdots, n - 1$.

Here, the first 4th root is selected for each domain, in which $\text{Re}(\beta_j) > 0$, and $\text{Im}(\beta_j) < 0$.

Consider the boundary conditions at infinite distance from moving load. When x tends to $-\infty$, the factors $e^{\lambda_{1,n}x}$ corresponding to the terms with $n = 3, 4$ tend to infinity. Likewise, when x tends to $+\infty$, the factors $e^{\lambda_{2,n}x}$ corresponding to the terms with $n = 1, 2$ tend to infinity. Therefore, applying the boundary conditions results in $A_2 = A_4 = B_1 = B_2 = 0$. Superimposing the homogeneous and the particular solutions leads to the general solutions of the beams. Thus, the system solution in Fourier domain reads

$$\widetilde{w}_1(x,\omega) = A_1 e^{\beta_1 x} + A_2 e^{i\beta_1 x} + \frac{-Fv^3 e^{-i\omega x/v}}{EI(\omega^4 - \beta_1^4 v^4)}, \qquad x \leqslant x_{tp}, \qquad (2.14\text{a})$$

$$\tilde{u}_1 = \frac{(ic_{t,1}\omega + k_{t,1})}{(-\rho_{t,1}\omega^2 + ic_{t,1}\omega + k_{t,1})} \widetilde{w}_1, \qquad x \leqslant x_{tp}, \qquad (2.14\text{b})$$

$$\widetilde{w}_2(x,\omega) = B_3 e^{\beta_2 x} + B_4 e^{i\beta_2 x} + \frac{-Fv^3 e^{-i\omega x/v}}{EI(\omega^4 - \beta_2^4 v^4)}, \qquad x \geqslant x_{tp}, \qquad (2.14\text{c})$$

$$\tilde{u}_2 = \frac{(ic_{t,2}\omega + k_{t,2})}{(-\rho_{t,2}\omega^2 + ic_{t,2}\omega + k_{t,2})} \widetilde{w}_2, \qquad x \geqslant x_{tp}. \qquad (2.14\text{d})$$

The unknown complex constants $A_{1,2}$ and $B_{3,4}$ are found by substituting the Equation 2.14a and Equation 2.14c into the following Fourier interface conditions;

$$\widetilde{w}_1(x_{tp}, \omega) = \widetilde{w}_2(x_{tp}, \omega), \qquad (2.15\text{a})$$

$$\widetilde{w}_1'(x_{tp}, \omega) = \widetilde{w}_2'(x_{tp}, \omega), \qquad (2.15\text{b})$$

$$\widetilde{w}_1''(x_{tp}, \omega) = \widetilde{w}_2''(x_{tp}, \omega), \qquad (2.15\text{c})$$

$$\widetilde{w}_1'''(x_{tp}, \omega) = \widetilde{w}_2'''(x_{tp}, \omega). \qquad (2.15\text{d})$$

The solutions then can be achieved in the space-time domain by applying the

inverse Fourier transform to the Equation 2.14;

$$w_j(x,t) = \frac{1}{2\pi} \int\limits_{-\infty}^{\infty} \widetilde{w}_j(x,\omega) e^{i\omega t} \mathrm{d}\omega \tag{2.16a}$$

$$u_j(x,t) = \frac{1}{2\pi} \int\limits_{-\infty}^{\infty} \tilde{u}_j(x,\omega) e^{i\omega t} \mathrm{d}\omega. \tag{2.16b}$$

The integrands being involved, the solutions are derived numerically, as in the thesis by (Faragau 2017)[2].

Now consider the same system without any mitigation measure—no TMD. It is referred to the *nominal track* throughout this document. Ignoring the TMD, its solution can be derived through the same procedures discussed in the current subsection 2.2.3.

2.2.4   Transition radiation

The interaction of load (with uniform rectilinear motion) and inhomogeneity leads to radiation in the form of elastic wave as a characteristic source of vibrations. This phenomenon is known as *transition radiation* (Vesnitskii and Metrikin 1992)[3] and explained further as follows (Van Dalen et al. 2015). As seen earlier, the solution of each semi-infinite beam consists of two parts, namely the particular solution and the homogeneous solution. The former is associated to the steady-state regime while the latter to the free field.

Considering the load velocity being subcritical[4] in the steady-state regime, the response is called *eigenfield*. It is stationary, accompanied by, and (in the absence of damping) symmetric with respect to the moving load. Mathematically, in the general solution (Equation 2.16), this situation can be achieved by choosing the position of moving load, $x = vt$, far from the transition point where the eigenfield is not affected by inhomogeneity. Doing so, the homogeneous solution becomes zero[5].

---

[2]All credit goes to Ir. Faragau for the MATLAB code of the numerical integration.

[3]This was the first study to evaluate the transition radiation in the context of mechanical systems; originally, this phenomenon was proposed within the framework of electromagnetism by (Ginzburg and Frank 1945).

[4]The load velocity is smaller than the minimum phase velocity; there is no wave propagation in the nominal track.

[5]Alternatively, same situation can be considered in the near field simply by equating the foundations stiffness to the desired domain, $k_1 = k_2$.

Upon approaching and passing the transition point from the soft track to the stiff track, the transient solution is deformed compared to the eigenfield and develops into a new eigenfield corresponding to the mechanical properties of the stiff track. This discrepancy in the eigenfields before and after x_{tp} is attributed to the source of transition radiation. It is the homogeneous solutions of the system that capture the radiation fields; they detach themselves from the load and propagate independently toward the infinities. Therefore, they are referred to as *free fields*.

2.3 TMD optimization

To suppress the vibrations, the TMDs parameters are tuned through a numerical optimization method. In general, many choices are available with regard to the optimization that can be considered according to their advantages and disadvantages to solve a specific problem. Herein, a population-based and metaheuristic optimization method, *evolutionary algorithm* (EA), is adopted due to its flexibility and simplicity (Al-Salami 2009). In this section, mathematical optimization is overviewed based on the textbook (Kochenderfer and Wheeler 2019). Then, the adopted EA (Deb et al. 2002), *nondominated sorting genetic algorithm type two* (NSGA-II), is briefly discussed in regard to tuning the TMDs parameters.

2.3.1 Multiobjective optimization, NSGA-II

Note that the TMDs parameters are referred to *design variables/points* while the criteria to be minimized are called *objective functions*. The functions can be dynamic responses in Fourier or time domain, the difference between the soft and the stiff tracks' wavenumbers, the energy radiations (free fields) along the structure, and generally, any desired mathematical function that is interrelated with the design variables/points. The optimization is discussed as follows.

Consider a *design point*, p, from the mathematical domain of the *objective function*, $f(p)$. In the context of optimization, the point, p^*, is called a *solution/minimizer* for which f is minimized (has minimum value). In general, an optimization problem reads

$$\min_{\mathbf{p}} \quad f(\mathbf{p})$$
$$\text{subject to} \quad \mathbf{p} \in P, \tag{2.17}$$

where the design point $\mathbf{p}$ can be a vector of n dimensions consisted of n design variables from a *feasible* space, P, with the solution $\mathbf{p}^*$. Objective ranking can be

15

assigned to two points $\mathbf{p}$ and $\mathbf{p}'$; that is, the point $\mathbf{p}$ is a better solution than $\mathbf{p}'$ if the scalar value of $f(\mathbf{p})$ is smaller than $f(\mathbf{p}')$.

Note that EAs seek multiple solutions by simultaneously distributing many design variables from the feasible spaces, randomly and iteratively. Moreover, the EAs can overcome multiple objective functions with *conflicting* interests. To clarify, consider a bicriteria optimization, for example, in designing process of a concrete cantilever beam with a constant cross-section; conflicting objectives can be maximizing the load-carrying capacity of the beam (to meet the standards in structural codes) while simultaneously minimizing the cross-section's area, to reduce cost of fabrication.

Now consider a problem with multiple functions. In general, the point $\mathbf{p}$ *dominates* the point $\mathbf{p}'$, if $\mathbf{p}$ is better than $\mathbf{p}'$ in at least one objective function (smaller value of f) and no worse in all other functions (smaller or equal value of f). Notice that $\mathbf{p}$ can be better for some functions while $\mathbf{p}'$ for some others. Therefore, there does not exist a single so called best solution from among many other solutions, and trade-off is required based on the designer's criteria.

In the presence of multiple functions, understanding of *Pareto optimality* is valuable. It describes a notion where no objective can be improved without deteriorating at least one other objective. It is named after the Italian civil engineer, Vilfredo Pareto. Likewise, if a point $\mathbf{p}$ is to be improved for an objective function, the others are worsen (larger value of f); the set consisting of these points is called *Pareto optimal*. The scalar values of the objective functions corresponding to the aforementioned points, all together, is called *Pareto frontier/curve*[6].

As mentioned earlier, NSGA-II is considered for tuning the TMDs parameters. Note that the *genetic algorithm* is an EA that mimics the natural selection in the biological evolution[7]. Initially, it is discussed for a single objective function and then is extended for multiple functions in NSGA-II as follows.

In the genetic algorithm with one objective function, the *individuals/genomes* (design points in n dimensions, here $n = 6$) with better objective values have better reproduction fitness. Each individual has its own specific chromosomes made of *genes* ($\rho_{t,1}$, $\rho_{t,2}$, $k_{t,1}$, $k_{t,2}$, $\zeta_{t,1}$, $\zeta_{t,2}$). Following the biological evolution, the fitter individuals in the current generation are considered as parents to pass on their genes to their offspring who are basically the population of next generation. To

---

[6]Recall that the evolutionary algorithms are population-based methods; thus, they spread the populations over the Pareto frontier.

[7]It is worthwhile to know that an organism's complete set of DNAs is called *Genome*. The *Chromosomes* are consisted of DNAs and the DNAs are again consisted of the *Genes*; loosely speaking, Genome > Chromosome > DNA > Gene.

do so, using the *binary Tournament Selection*, out of 2 randomly selected parents, the fittest one is chosen. This process is repeated for each parent separately. Next, these parents go through certain biological operations to pass on their genes by forming their offspring;

- *crossover* children are born by combining the genes of two parents;

- to consider the new traits which might never have been in the initial population, new genes from the design space are again randomly selected to be incorporated into the single parents' chromosomes—these are *mutation*[8] children.

In the NSAG-II optimization where multiple functions can be considered, an initial population of N individuals is randomly sampled throughout the design space. Then, N parental *pairs* are listed[9] and the N fittest ones are identified through the tournaments. Thereafter, the crossover and mutation are performed over the selected parents to create the *initial generation*.

The procedure for creating the next generations, however, is slightly different; the selection criterion after the usual tournaments is now based on the *crowded-comparison operator* (Deb et al. 2002), with which the *diversity* in the population is considered (set of points with larger distance from each other). This time the parents in the initial generation survives (*elitism*) together with their own children to form a population twice the initial size. The nondominated points/individuals are now sorted according to their *nondomination ranking*[10], to form the frontier accordingly. Then the best solutions are adopted in the order of their *ranks* and according to their *crowding distances*, until the population size is reduced to N as the next generation. The preferred solutions within the last level/rank are those which are less crowded by other solutions; this is in favor of having a wider spread of solutions (better diversity). The same approach is repeated for creating the next generations until the algorithm converges to the best nondominated frontier.

---

[8]To clarify, the advent of blue eye's color in human beings can be mentioned as an example of mutation (Eiberg et al. 2008); a specific trait which was already absent becomes to existence.

[9]Identical parents might appear.

[10]The individuals within the 1st level are not dominated by any others (the best fitness rank); similarly, the individuals in the 2nd level are not dominated by any others except those in level 1; likewise, the individuals in the 3rd level are not dominated by any others except those in the level 1 and 2; and so forth.

2.3.2   Objective functions

The amplified transient vibrations are normally attributed to the abrupt change in the track stiffness as one of the main factors. This can be associated to different mechanical properties in the wavenumbers of the soft and the stiff tracks in Equation 2.9a. Therefore, the goal is to suppress the amplified response through tuning/optimizing the TMDs parameters (design variables/points) such that this discrepancy (objective function) is minimized. Mathematically, two complex wavenumbers are equal if and only if $\mathrm{Im}(\beta_1) = \mathrm{Im}(\beta_2)$, *and* $\mathrm{Re}(\beta_1) = \mathrm{Re}(\beta_2)$. Consequently, the optimization problem with two objective functions and six design variables is formulated as[11]

$$
\begin{aligned}
\min_{\mathbf{p}} \quad & f_1(\mathbf{p}) = |\mathrm{Im}(\beta_1) - \mathrm{Im}(\beta_2)| \\
\min_{\mathbf{p}} \quad & f_2(\mathbf{p}) = |\mathrm{Re}(\beta_1) - \mathrm{Re}(\beta_2)| \\
\text{and} \quad & 1 \leqslant \{p_1, p_2\} \leqslant 500 \\
& 1\mathrm{e}7 \leqslant \{p_3, p_4\} \leqslant 1\mathrm{e}9 \\
& 0.05 \leqslant \{p_5, p_6\} \leqslant 1.5,
\end{aligned}
\tag{2.18}
$$

where $\mathbf{p}$ is a 6-dimensional point consisted of 6 design variables of the TMDs; variables' bounds corresponding to p_n, $(n = 1, ..., 6)$, represent the real-valued $\rho_{t,j}$, $k_{t,j}$, and $\zeta_{t,j}$, respectively—see subsection 2.4.1.

Finally, the choice of frequency in the objective functions completes the optimization problem. Note that the amplified vibrations in the continuous system are naturally attributed to a range of frequencies. On the other hand, the imaginary and real parts of the wavenumbers should be evaluated at an identical frequency. Therefore, the tuned frequency in Equation 2.18 is considered only for a specific load velocity as follows. Consider the spatial point in the soft track, $x_{\max}$, where the *maximum transient displacement* occurs, $w_1(x_{\max}, t)$; the frequency for which $|\widetilde{w}_1(x_{\max}, \omega)|$ is maximum (peak frequency), is considered as the tuned frequency, ω_{opt}, with which the optimization is performed. The adopted values of the corresponding parameters are discussed in subsection 2.4.1.

Due to low computational cost, the population size and maximum number of generations are selected as 3000 and 1500, respectively. The performance measure of the optimization is considered through a convergence metric defined in the same article (Deb et al. 2002). It is based on the crowding distance and the uniformity

---

[11]No constraint is considered for the optimization problem.

measure of the solutions in the frontier. At best, this metric is zero where the nondominated solutions are spread most uniformly. Considering the large values being selected for both population size and number of iterations, the change of the convergence metric between the last frontier and previous ones is extremely negligible, meaning the last frontier cannot be noticeably improved further.

2.4 Results and discussions

Initially, the numerical values selected for the mechanical parameters are discussed in this section. The *tuned* design variables, derived through NSGA-II optimization, are then presented and discussed. Subsequently, the systems' dynamic analyses are investigated through the results corresponding to the dispersion relations, displacements in time domain, Fourier amplitude spectrum, and energy.

2.4.1 Choice of the parameters

Superstructure and substructure

Due to symmetry in the corss-section of the track, only half of the structural components are incorporated into the one-dimensional mechanical system. That is, one rail and half of the sleeper length and of all other elements within the track width. The beam linear density, ρ, is consisted of the rail (UIC60) linear mass, 60 kg/m, together with effective mass of the sleeper per unit length, $\rho_s = 250/2/0.6$ kg/m (Fărăgău, Mazilu, et al. 2021); $s_{\mathrm{sb}} = 0.6$ m is the sleeper bay spacing. Moreover, vertical stiffness and damping of the components are serially coupled to represent the Kelvin foundation. Note that the stiffness of the concrete sleeper is ignored due to its significantly large magnitude. Furthermore, the foundation's damping ratio, $\zeta = 0.05$, is kept constant at any spatial point along the track[12].

Stiffness ratio and load velocity

The stiffness ratio, $s_r = k_2/k_1$, and load velocity play active roles in the undesired behavior at transition zone. These values are selected based on (ibid.). Even though the stiffness ratio of 5 is rare in practice, its choice results in stronger

---

[12]See (Rodrigues 2017) for further information regarding the track modeling and the corresponding parameters.
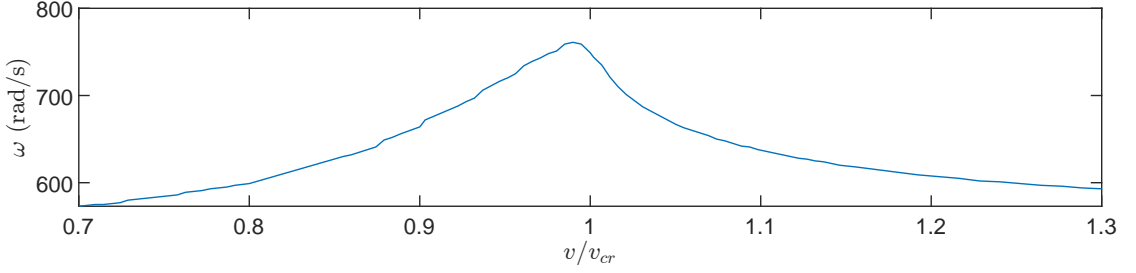
Figure 2.2: The frequency at which $|\widetilde{w}_1(x_{\max}, \omega)|$ is maximum (peak frequency) for various relative velocities. $x_{\max}$ is the spatial point in the soft track where the transient displacement is maximum, $w_{1,\max} = w_1(x_{\max}, t)$.

and more evident vibrations; hence, simpler distinction of the mechanisms of the transition radiation.

Normally, in practice, $60 - 70\%$ of the critical velocity is considered as the train's operative speed in the soft tracks. On the other hand, if the speed (not the relative velocity) corresponding to this range is adopted for the current mechanical model, the results would be correspondent to those of the speed of about 10% of the measured critical velocity in practice. This is because of the larger critical velocity introduced by Kelvin foundation in which the substructure mass is not accounted for (Fărăgău, Mazilu, et al. 2021). Therefore, the analyses herein are evaluated based on *relative velocity*; load velocity relative to the critical velocity of the system.

Consider the critical velocity, v_{cr}, corresponding to the soft track in the nominal system. Despite the aforementioned limitation, often a range of relative velocities close to, but smaller than v_{cr} is considered. In doing so, the Cherenkov radiation is avoided (Wolfert 1999), and yet it is large enough to amplify the vibrations in favor of easier identification of the transition radiation mechanisms. Note that the large magnitude of v does not lead to unrealistic results as they are eventually attributed to the relative velocity, v/v_{cr}. Following the discussion in subsection 2.3.2, the optimization problem is performed for $v/v_{cr} = 0.95$. Therefore, the frequency $\omega_{\mathrm{opt}} = 720$ rad/s is considered for the optimization according to Figure 2.2 where ω_{opt} is plotted for various relative velocities.

The TMDs parameters

The optimization problem in Equation 2.18 requires numerical bounds for design variables corresponding to TMDs. On the other hand, in the context of tuned mass dampers at transition zone, the overall range of design values is not well known yet. Therefore, it is worthwhile to briefly investigate the *rail vibration damper*, also known as TMD (Xiao et al. 2017), to have a rough and initial estimation of

Table 2.1: List of the mechanical parameters.

Parameters	Magnitude	Dimension	Definition
EI	6.42e6	N/m^2	rail bending stiffness
F	8e4	N	constant load amplitude
v_{cr}	415.2	m/s	critical velocity (nominal soft track)
s_{sb}	0.6	m	sleeper bay spacing
s_r	5	−	stiffness ratio, k_2/k_1
ρ	268.33	kg/m	beam linear mass
k_1	8.33e7	N/m^2	distributed static stiffness, soft track
k_2	4.165e8	N/m^2	distributed static stiffness, stiff track
ζ	0.05	−	foundation's damping ratio
$\rho_{t,j}$	$1-500$	kg/m	range of the TMDs' linear mass
$k_{t,j}$	1e7 − 1e9	N/m^2	range of the TMDs' static stiffness
$\zeta_{t,j}$	$0.05-1.5$	−	range of the TMDs' damping ratio

the aforementioned bounds. It should be stressed that the TMD analysis herein is *not* limited to rail dampers, as they belong to different principles. In fact, rail dampers are relatively well established for suppressing vibrations with regard to the sound radiation in the rails.

The rail vibration damper consists of the mass which is connected to the rail foot and web by an elastomeric material that accounts for both elasticity and viscosity. The elastomeric component is modeled by a vertical spring and a dashpot which are connected to the rigid mass from the top and to the beam from the bottom. The rail dampers are normally tuned to suppress the pinned-pinned vibrations[13] of the rail (ibid.). Considering the loss factor[14] of rail dampers, an approximate range of 0.1-1.3 can be found in (Kuchak et al. 2021; Wu 2008; Xiao et al. 2017). In addition, an overall range of 37-592 MN/m can be attributed to the stiffness parameter of rail dampers according to (Jin, Kim, et al. 2022; Jin, W. Yang, et al. 2020; Wu 2008; Xiao et al. 2017). Moreover, a range of 9-18 kg/m was recommended for the linear mass by (W. Li et al. 2021).

Therefore, the intervals 0.05-1.5 and 6-600 MN/m are respectively selected for the damping ratio and the stiffness of TMDs. However, a significantly larger upper bound is adopted for the corresponding linear mass, as the vibrations in transition

---

[13]The standing wave modes of the rail where the fasteners at the sleepers behave like hinged supports.

[14]The loss factor, η, and damping ratio can be related through $\eta \approx 2\zeta$ (Krylov 2001).

zone are stronger than those regarding the sound radiations in rail. It should be clarified that herein, the TMD feasibility, in theory, is of interest and not much of the physical designs in practice. Therefore, the type of TMD material, and their installing locations across or along the track are considered *conceptually*[15]. Having said that, the magnitude of 500 kg/m is selected as the high end of $\rho_{t,j}$ in Equation 2.18. Finally, the mechanical parameters and their values are presented in Table 2.1.

Table 2.2: The TMDs optimized parameters.

Parameters	k_t (N/m^2)	ρ_t (kg/m)	ζ_t
Soft Track	7.5771e7	188.12	0.8007
Stiff Track	5.2866e8	461.05	0.1217

2.4.2 TMDs' optimized values

As discussed in section 2.3, there are multiple solutions in the converged Pareto frontier that can be traded off based on the desired criteria. In the selection of the final solution, the criterion is to attribute equal weight to both objective functions in Equation 2.18. The design values of the chosen solution corresponding to the *tuned* mass dampers are presented in Table 2.2, and the corresponding wavenumbers are plotted against the frequency in Figure 2.3.

According to Figure 2.3, the wavenumbers corresponding to the optimized track demonstrate zero difference at the tuned frequency $\omega_{\text{opt}} = 720$, as expected. This reduction can also be signified for frequencies close to the tuned frequency. In contrast, the difference in the imaginary part adversely indicates an increase at frequencies close to 418 rad/s, due to addition of TMD. This increase is significantly larger at higher frequencies. Note that the algorithm approached to a more realistic value for the TMD mass in the soft track, $\rho_{t,1} = 188.12$ kg/m (0.7 times smaller than the beam element), compared to that of the stiff track, $\rho_{t,2} = 461.05$ kg/m (1.72 times larger than the beam element).

---

[15]For example, the TMDs can be installed on the sleepers, main rails, external rails, etc; this research is not focused on this matter.
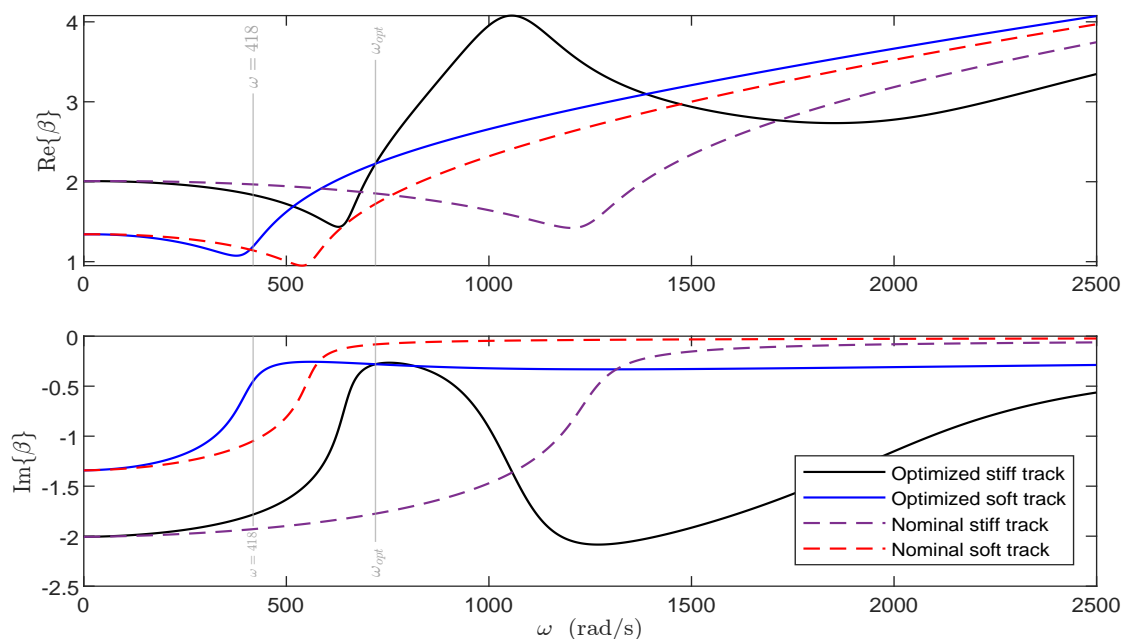
Figure 2.3: Comparison of the wavenumbers' difference between the soft and the stiff tracks with and without TMDs. ω_{opt} is denoted by the vertical dash-dotted line.

2.4.3   Dispersion analysis

To have a better understanding of the system's dynamic behavior with regard to the employment of TMDs, the waves dispersion which might propagate along the infinite beam (Shamalta and A. Metrikine 2003) are evaluated.

Note that in dynamic analyses of the system with and without TMDs, the steady-state responses are derived by considering the load in the *far field* space, in Equation 2.14. That is, the steady-state solution is not derived by a separate set of EOMs. It is, however, conceptually and briefly recognized in this subsection to derive the dispersion relation as follows.

Consider the *homogeneous form* of the system with TMDs. Forward Fourier transform is applied to the correspondent EOMs over time and space (ibid.);

$$\widetilde{w}(\beta,\omega) = \int\limits_{-\infty}^{\infty}\int\limits_{-\infty}^{\infty} w(x,t)e^{i(\omega t-\beta x)}\mathrm{d}x\mathrm{d}t, \tag{2.19a}$$

$$w(x,t) = \frac{1}{(2\pi)^2}\int\limits_{-\infty}^{\infty}\int\limits_{-\infty}^{\infty} \widetilde{w}(\beta,\omega)e^{-i(\omega t-\beta x)}\mathrm{d}\beta\mathrm{d}\omega. \tag{2.19b}$$

23

The term corresponding to the load reads

$$- \int\limits_{-\infty}^{\infty} F\delta(x - vt)e^{-i\beta x}\mathrm{d}x = -Fe^{-i\beta vt}, \tag{2.20a}$$

$$- \int\limits_{-\infty}^{\infty} Fe^{-i\beta vt}e^{i\omega t}\mathrm{d}t = -2\pi F\delta(\omega - \beta v). \tag{2.20b}$$

The kinematic invariant can be found as $\omega = \beta v$ which is attributed to the load and the argument of the Dirac-Delta function. The derivation is continued by rewriting the equations in its matrix form as follows.

$$\begin{bmatrix} EI\beta^4 - \rho\omega^2 + i(c+c_t)\omega + k + k_t & -ic_t\omega - k_t \\ -ic_t\omega - k_t & -\rho_t\omega^2 + ic_t\omega + k_t \end{bmatrix} \begin{bmatrix} \widetilde{w}(\beta,\omega) \\ \tilde{u}(\beta,\omega) \end{bmatrix} = \begin{bmatrix} -2\pi F\delta(\omega - \beta v) \\ 0 \end{bmatrix}, \tag{2.21}$$

$$\tilde{\mathbf{W}} = \mathbf{D}^{-1}\tilde{\mathbf{F}}, \tag{2.22}$$

$$\mathbf{W}(x,t) = \frac{1}{(2\pi)^2} \int\limits_{-\infty}^{\infty} \int\limits_{-\infty}^{\infty} \frac{\mathbf{N}(\beta,\omega)}{\det(\mathbf{D})}\mathrm{d}\beta\mathrm{d}\omega, \tag{2.23}$$

$$\mathbf{N}(\beta,\omega) = \mathrm{adj}(\mathbf{D})(-2\pi F\delta(\omega - \beta v))e^{-i(\beta x - \omega t)}, \tag{2.24}$$

$$\det(\mathbf{D}) = (EI\beta^4 - \rho\omega^2 + i(c + c_t)\omega + k + k_t)(-\rho_t\omega^2 + ic_t\omega + k_t)$$
$$- (ic_t\omega + k_t)^2, \tag{2.25}$$

where $\mathbf{D}$ is the dynamic stiffness matrix—the first matrix in the left side of Equation 2.21. The dispersion relation is Equation 2.25 equated to zero;

$$\det(\mathbf{D}(\beta,\omega)) = 0, \tag{2.26}$$

where its roots are the poles of the integral in Equation 2.23. Likewise, it can be obtained for the nominal track.

To plot the *dispersion curves*, damping constants are zeroed out, in which the dispersion equation (Equation 2.26) is satisfied for *real* pairs of β and ω (Shamalta and A. Metrikine 2003; Wolfert 1999). Substitution of the kinematic invariant ($\omega = \beta v$) results in a polynomial of order 6 (it is 4th order for the nominal system). Dispersion curves are therefore plotted against both frequency and wavenumber in Figure 2.4, which are illustrated by dark red and dark blue colors for the nominal and optimized tracks, respectively.

Note that the curves appear in pairs in $\pm\omega$ which are shown only for positive frequencies in Figure 2.4. Moreover, the kinematic invariant is signified by the
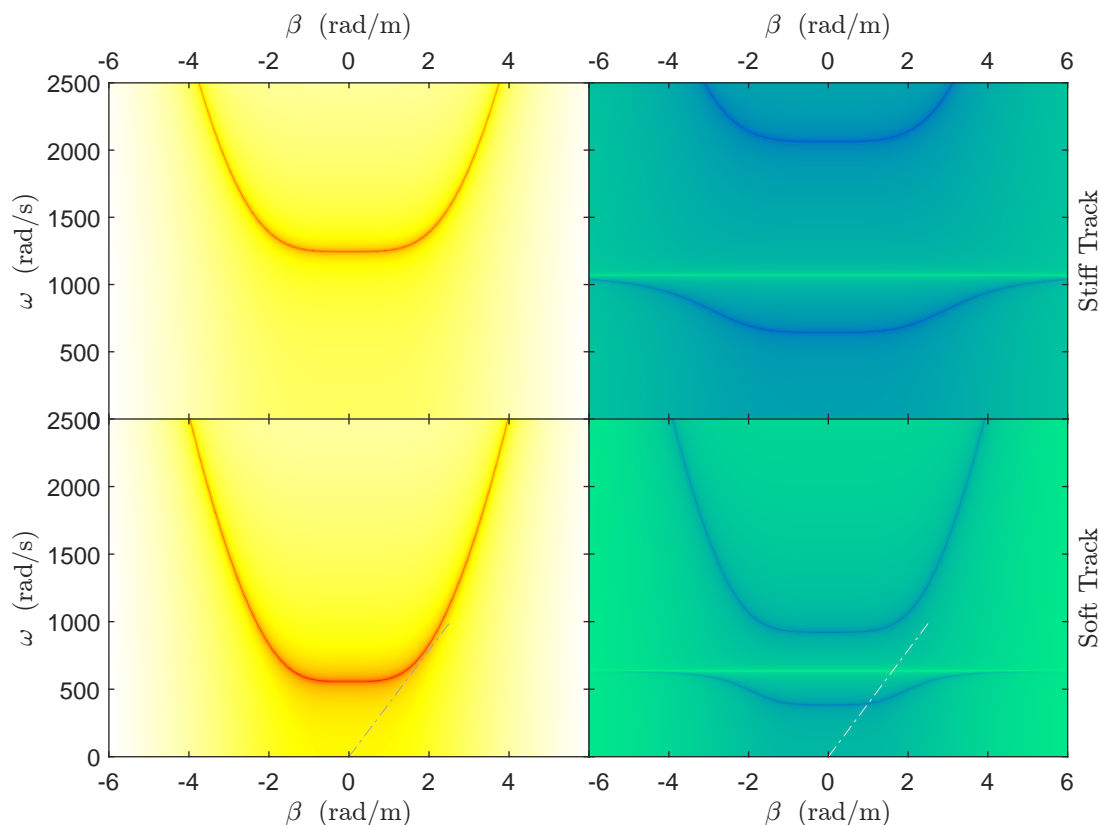
Figure 2.4: Dispersion curves of the nominal system (red curves) and the optimized system with TMDs (dark blue curves). The kinematic invariant (dash-dotted line) is correspondent to $0.95v_{cr}$. v_{cr} is the critical velocity corresponding to the nominal soft track.

dash-dotted line corresponding to $0.95v_{cr}$ of the nominal soft track. Furthermore, the range of frequency where no propagation exist is known as the *stop band*, otherwise it is *pass band* which are separated by *bounding frequencies*[16] (Fărăgău, Oliveira Barbosa, et al. 2022; Xiao et al. 2017).

Consider the range of frequencies where the pass band of the soft track is in the stop band of the stiff track in the nominal system. This is the main difference between the dispersion curves corresponding to both domains. Noticeably, addition of TMDs results in new stop bands in both domains. The stop band in the soft track is almost within the same range of frequencies for which the objective functions (the difference in wavenumbers corresponding to the soft and the stiff tracks) in Equation 2.18 exhibit significant reduction, as can be seen in Figure 2.3 (note that this comparison is conceptual as damping was neglected).

Consider the dispersion curve with horizontal asymptote corresponding to the

---

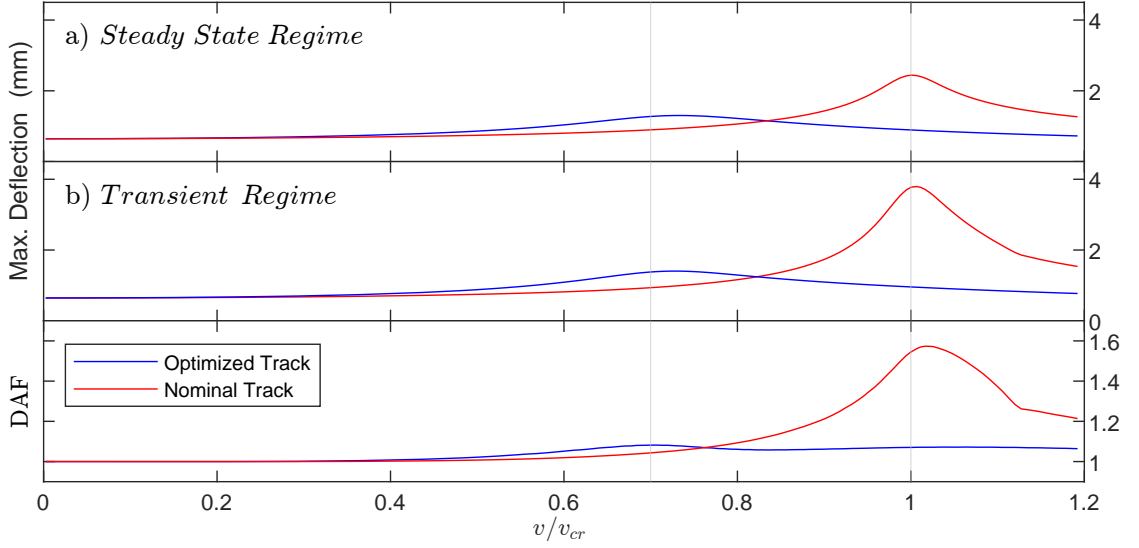[16]It is also called the *cutoff frequency*.

Figure 2.5: DAF and maximum displacements of the track with and without TMDs in the steady-state and transient regimes. v_{cr} is the critical velocity in the nominal soft track.

soft track with TMD. Notice that the kinematic invariant with any slope (except zero) always crosses the dispersion curve at one point. This is correspondent to the free propagating wave in the system with TMD. At load velocity $v = 0.95v_{cr}$, the tangent of crossing point (group velocity at 397 rad/s) is smaller than the kinematic invariant slope ($\omega = \beta_1 v$), meaning the propagating wave is behind the load.

2.4.4   Displacements in time domain

The amplified response at transition zone can be associated to maximum displacement in the soft track. Therefore, to clarify the mechanisms of mitigation measure corresponding to TMD, dynamic amplification factor, DAF, of the optimized system is evaluated in this subsection.

The DAF is defined as the ratio of maximum transient displacement to the maximum steady-state displacement of the soft track at each relative velocity;

$$\text{DAF} = \frac{\max\left\{w_{1,\text{transient}}(x,t)\right\}}{\max\left\{w_{1,\text{steady-state}}(x,t)\right\}}. \tag{2.27}$$

The DAF curves are presented for both nominal and optimized systems in Figure 2.5. The results of the optimized track are discussed compared to the nominal track, as follows.

Due to addition of TMD, maximum displacements in both steady-state and transient regimes illustrate significant reductions at load velocity for which the optimization was performed ($v = 0.95v_{cr}$, related to $\omega_{\mathrm{opt}} = 720$ rad/s of the nominal soft track) as well as the corresponding neighboring velocities, as expected. Clearly, this is echoed by noticeable reduction in DAF at the aforementioned relative velocities.

The DAF peak represents the system's critical velocity. Hereafter, the critical velocity corresponding to the system with TMDs is signified by v_t. In fact, due to application of TMDs, the nominal system with load velocity $v = 0.95v_{cr}$ in *subcritical regime* changes to an optimized system with load velocity $v \approx 1.48v_t$ in *supercritical regime*, through a shift in the DAF peak to a smaller value at $v_t \approx 0.64v_{cr}$. Note that this behavior is not desired and should be avoided, even though favorably, the amplification indicates considerable decrease.

Additionally, the displacement fields at different time moments are presented for both systems in Figure 2.6. Panel (a) illustrates the eigenfields in the left domain upon reaching the transition point, x_{tp}. Notice the free propagative wave behind the load which signifies the optimized track being in supercritical regime, as discussed earlier; this is correspondent to the point at which the kinematic invariant ($\omega = \beta_1 v$, $v = 0.95v_{cr}$) crossing the lower dispersion curve in the optimized soft track, as can be seen in (Figure 2.4). In addition, due to presence of damping in the foundation (Dieterman, V. Metrikine, et al. 1997), the maximum displacements of the eigenfields are not exactly under the load, but slightly behind it.

Deformations in displacement fields can be signified by approaching the inhomogeneity in panel (b) while the amplified response indicates the maximum transient displacement in panel (c). This is considerably smaller for the optimized track echoing the results in Figure 2.5, due to the TMDs being *tuned* for the frequency ω_{opt} corresponding to this amplified response in the nominal track. After passing x_{tp}, the optimized system demonstrates a less intensified fluctuation compared to the system without TMD, see panels (d) and (e). Then, the free fields[17] gradually being detached from the load, are propagating leftward in the left domain[18], see panels (f) and (g). Afterward, in panel (h), both systems illustrate the eigenfields at the steady-state regime far enough from the transition point in the stiff domain. Notice that the tail (free propagative wave) in the system with TMD does not interact with the inhomogeneity anymore while the free fields are still propagating to a less degree.

---

[17]Recall that the free fields are correspondent to homogeneous parts of the general solutions, and the eigenfields are described by the particular solutions.

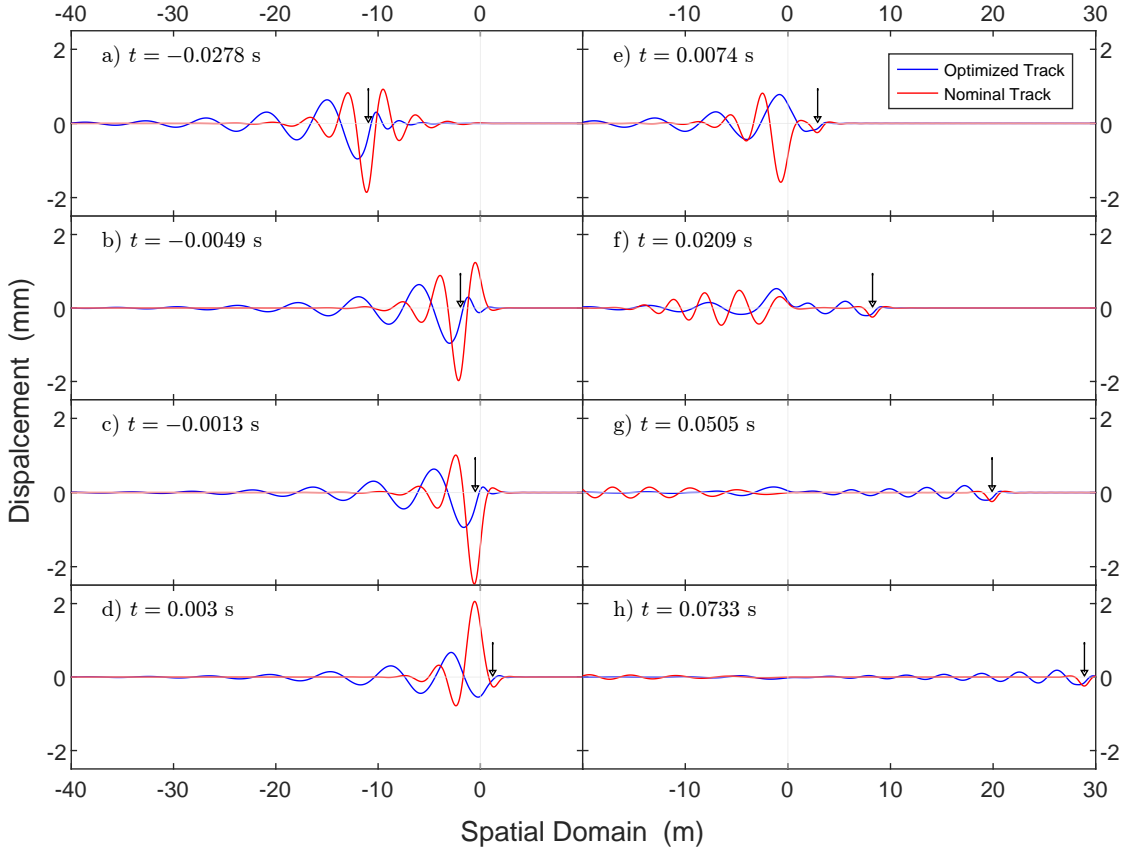[18]Also rightward in the right domain which is less evident.

Figure 2.6: Snapshots of the displacement fields at consecutive time moments for both nominal and optimized tracks. $v = 0.95\, v_{cr}$ corresponding to critical velocity of the nominal soft track. $x_{tp} = 0$ denotes the transition point.

2.4.5   Fourier amplitude spectrum

Fourier amplitude spectrum can provide the information on how the optimized system behaves at the tuned frequency, based on the wavenumbers' discrepancy (objective functions; $f_1 = |\mathrm{Im}(\beta_1) - \mathrm{Im}(\beta_2)|$, $f_2 = |\mathrm{Re}(\beta_1) - \mathrm{Re}(\beta_2)|$) in Equation 2.18.

Fourier displacements corresponding to the soft tracks with and without TMD in the steady-state regime are presented in Figure 2.7. Clearly, the Fourier contents demonstrate a shift in the peak corresponding to the nominal track to a lower frequency at $\omega = 418$ rad/s due to addition of TMD. This value is very close to the frequency[19] ($\omega = 397$ rad/s) at which the free wave propagates behind the load in the optimized system where the kinematic invariant crosses the dispersion

---

[19]Note that the damping was neglected in the dispersion analysis.

curve (Figure 2.4). It can be inferred that part of the energy close to the load is redistributed to the propagating wave, leading to a smaller amplitude under the load but a larger amplitude behind it, as can be seen in panel (a) of Figure 2.6.
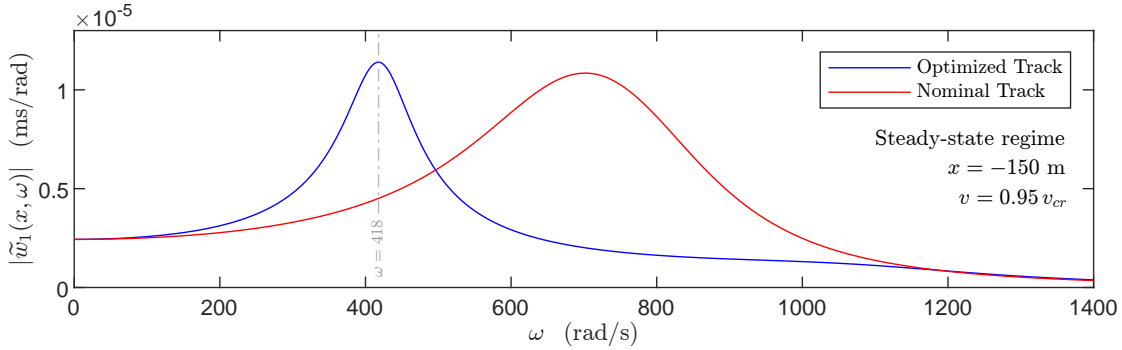
Figure 2.7: Fourier amplitude spectrum of the soft track at steady-state regime. The dash-dotted line signifies the peak frequency of the optimized track, $\omega = 418$ rad/s.
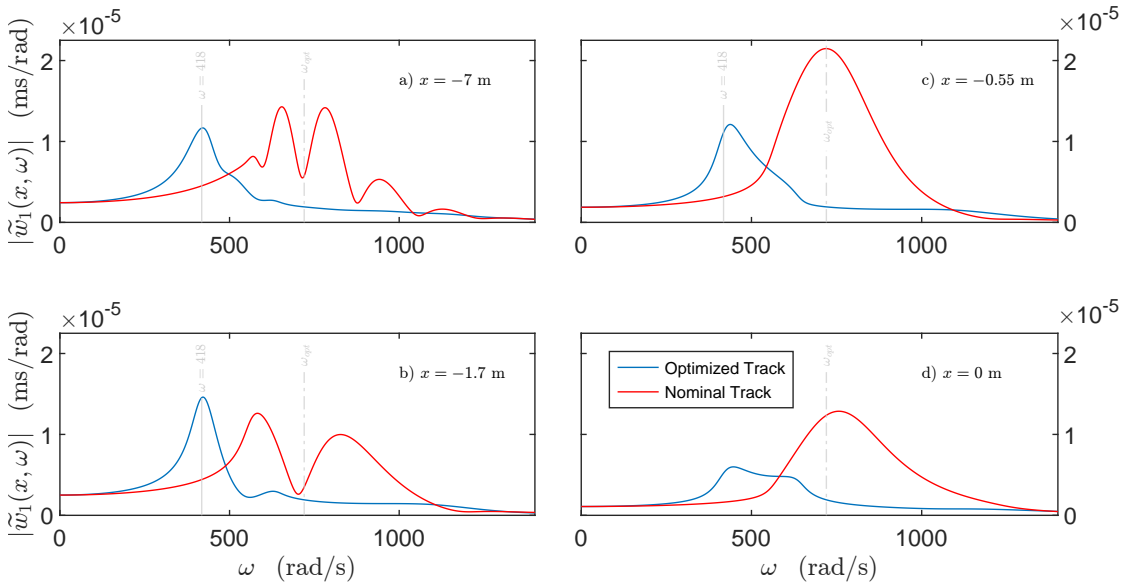
Figure 2.8: Fourier amplitude spectrum of the soft track at transient regime. The vertical solid line signifies the peak frequency ($\omega = 418$ rad/s) upon reaching the transition point. The dash-dotted line signifies $\omega_{\mathrm{opt}} = 720$ rad/s. Load velocity is 0.95% of the critical velocity corresponding to the nominal track.

Furthermore, the transient Fourier displacements corresponding to both systems for load velocity $v = 0.95 v_{cr}$, at various spatial points x, are presented in Figure 2.8. Consider the spatial point $x = -0.55$ m, where the nominal track exhibits an amplified response in time domain. Clearly, the Fourier content in the system with TMD demonstrates a significant reduction in amplitude at the

tuned frequency, as expected. Note that in the system with TMD, the peak frequency at $x = -7$ or $x = -1.7$ m indicates a shift to a slightly larger frequency at $x = -0.55$ m, in which the amplitudes are larger compared to the nominal track. This shift can be attributed to the same frequencies at which the objective function f_1, adversely indicates increase in magnitude (Figure 2.3).

2.4.6 Power input

The larger amount of energy being emitted to the railway track can be pertained to the bigger energy dissipation in the ballast layer, hence increase of degradation in the supporting structure (Fărăgău, Mazilu, et al. 2021; Sadri et al. 2019). Since the dissipated energy cannot be determined in the simplified model herein, the *power input* is considered instead. In doing so, the potential damage to the foundation can be assessed indirectly. The power input by the moving load reads

$$P(x = vt, t) = F\dot{w}(x = vt, t) \qquad \text{J/s}, \tag{2.28}$$

where $\dot{w}$ is the beam velocity at which the external load, F, is applied.

According to Figure 2.9, the steady-state power inputs are horizontal lines along the track; the bigger the slope of the rail under the load, the larger the power input (softer track). As the load approaches the transition point, the power inputs start to illustrate fluctuations through energy exchange between the moving load and the track. The peaks in both systems, close to the x_{tp}, are correspondent to the moving load which needs to impart extra energy into the track to pass the inhomogeneity while keeping its constant velocity.

Addition of TMDs leads to reduction in amplitude of the maximum peak which is more eventide for load velocity at which the TMDs were tuned ($v = 0.95v_{cr}$). Furthermore, the optimized track indicates an almost identical power input behavior for load velocities close to $0.95v_{cr}$ for which the DAF magnitudes are almost equal, as can be seen in Figure 2.2.

Afterward, the nominal track impart back noticeable energy to the external object, more specifically at positions close to $x_{tp} = 0$ (the trough). In contrast, the exchange energy between the load and the track is significantly reduced where the power input smoothly morphs to that of the steady-state in the stiff track.

More importantly, the effect of TMDs on the foundation damage can be indirectly evaluated through the *ratio* of maximum transient power input (maximum peak) to the steady-state power input in the corresponding domain. Addition of TMDs results in 35.2% reduction in the aforementioned ratio for $v = 0.95v_{cr}$; this
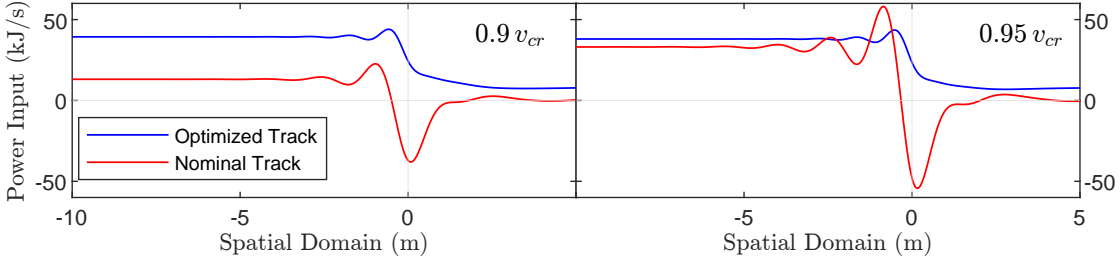
Figure 2.9: Power input of the tracks with and without TMDs at load velocities 0.9% and 0.95% of the critical velocity corresponding to the nominal track.

can be partly attributed to less damage to the foundation compared to the nominal track (Fărăgău, Andrei V Metrikine, et al. 2019).

2.4.7   Energy flux and spectral energy density

In this subsection, the influence of TMDs on energy radiation is evaluated through *energy flux*. To that end, the contribution of free field is considered only; due to presence of damping in the system (either by TMDs or foundation), the entire free field radiation can not be captured. Moreover, the free field energy distribution across the frequency spectrum can be examined through the *spectral energy density* relation.

Consider the *power flux* through a cross-section of the beam as (Wolfert 1999)

$$S_f(x,t) = \pm EI(w_f''' \dot{w}_f - w_f'' \dot{w}_f'), \tag{2.29}$$

where the subscript f denotes the free field propagating rightward for positive sign and leftward for negative sign. By integrating over time, the *total free field energy flux* for a given cross-section reads (Fărăgău, Andrei V Metrikine, et al. 2019; Wolfert 1999)

$$E_f(x) = \pm EI \int_{-\infty}^{\infty} w_f''' \dot{w}_f - w_f'' \dot{w}_f' \, \mathrm{d}t. \tag{2.30}$$

To consider the *spectral energy density* in Fourier domain, Equation 2.30 is reformulated in terms of frequency (in Appendix A) as follows (Van Dalen et al. 2015).

$$E_f(x) = \frac{\pm EI}{\pi} \int_{0}^{\infty} \mathrm{Re}\{\widetilde{w}_f''' \tilde{v}_f^* - \widetilde{w}_f'' \tilde{v}_f^{*'}\} \, \mathrm{d}\omega. \tag{2.31}$$

31

The integrand in the last equation is known as the spectral energy density, $E_s(x, \omega)$.
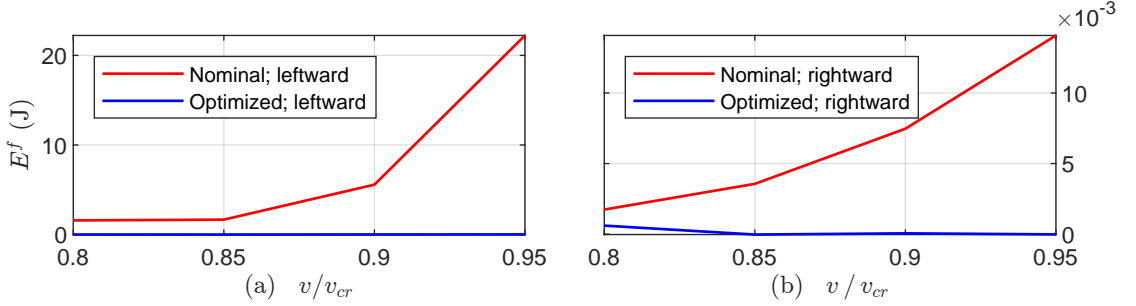

Figure 2.10: The energy flux for various relative velocities. The cross sections are chosen at $x = \pm 7.5$ m. The left panel is related to the leftward radiation and the right panel for the rightward radiation.
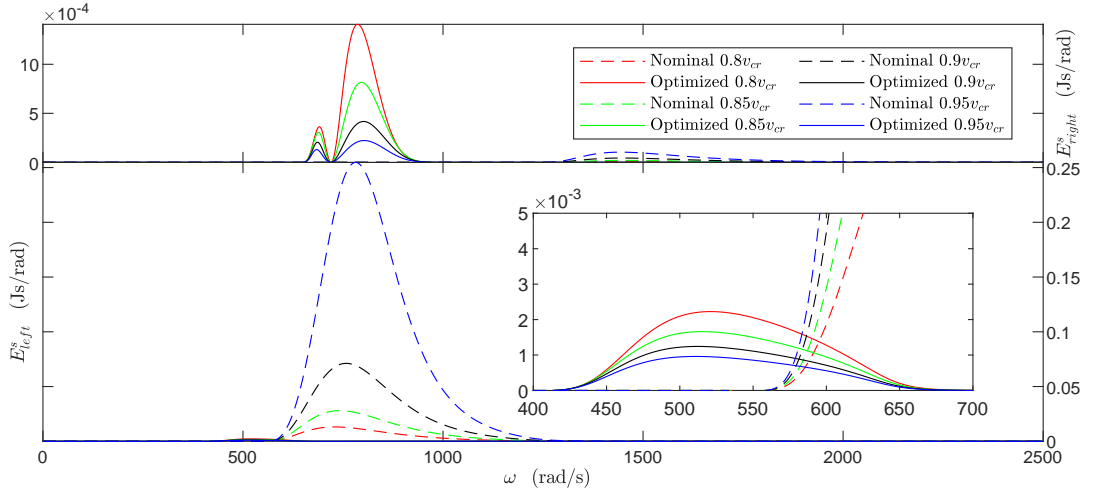

Figure 2.11: The spectral energy density of the tracks for multiple relative velocities at cross sections $x = \pm 7$ m. The bottom panel is related to the leftward radiation and the top panel to the rightward radiation.

The energy flux corresponding to the systems with and without TMDs for cross-sections at $x = \pm 7.5$ m are presented in Figure 2.10. Note that considering other spatial points can lead to slightly different results due to damping in the foundation and TMDs. As it can be seen, the leftward energy radiation in the soft domain is considerably larger than the rightward radiation in the stiff domain. In both cases, E_f indicates noticeable reduction for relative velocities closer to $v/v_{cr} = 0.95$ (corresponding to tuned frequency). This reduction possibly can be attributed to the large value of tuned damping ($\zeta_{t,1} = 0.8$) and strong counteracting forces between the beam and TMDs at transition zone. Furthermore, energy trap at transition zone might be another reason that can partly play a role in decreasing

the energy flux; this occurs when the free field energy is sustained longer, rather than radiating away from the transition point. This can be attributed to the wave propagating in positive x-direction, but slower than the load. This causes the wave to continuously be reflected at transition point. Herein, a negligible energy trap can be signified in panel (g) of Figure 2.6.

Furthermore, the spectral energy densities are plotted in Figure 2.11 for cross-sections at $x = \pm 7$ m. The leftward propagation in the bottom panel demonstrate completely flattened energy curves due to the employment of TMDs. On the other hand, there is a shift in the energy toward the lower frequencies with extremely small magnitudes. Considering the free field's rightward radiation, the addition of TMDs results in a shift in energy toward lower frequencies for all relative velocities in the top panel. Note that this shift is accompanied by increase in energy except at the frequency for which the TMDs were tuned. Note that this increase in energy is more evident for relative velocities other than $0.95v_{cr}$, as expected. Once again, the reduction in the wavenumbers' discrepancy at ω_{opt} is highlighted in accordance with the Figure 2.3.

Chapter 3

Auxiliary rail

To respond the second research question, the efficiency of auxiliary rail in improving the undesired behavior at transition zone is investigated in this chapter. Initially, previous studies are reviewed. Next, the incorporation of extra rail into the one-dimensional train-track model is briefly discussed. For the analyses throughout this chapter, two configurations are considered; first, addition of rails over soft track only, and second, extra rails over both soft and stiff tracks. Static stiffness behavior is then evaluated where a smoother transition is recognized for the first configuration. Moreover, following the same procedures in chapter 2, semi-analytical solutions are derived through Fourier transform method. Conclusions are established based on outcomes corresponding to dynamic amplification factor and power input. It is suggested that application of auxiliary rail leads to improvement in dynamic response of the track through increasing the critical velocity to a larger value.

3.1 Literature review

The available findings regarding the auxiliary rail are not as extensive as other mitigation measures. Overall, applying extra rails to the ballasted track can lead to uniform distribution of the load at transition zone (Indraratna et al. 2019). Although, less priority might be attributed to this solution compared to other mitigation measures when cost-effectiveness analysis is of interest (Read and D. Li 2006; Shan et al. 2013).

Extra rails are normally installed parallel to the original rails, inside and or outside of the track gauge. Extending the guard rails from the abutment of a bridge to its approach can be mentioned as an example where a better load distribution is achieved (Read and D. Li 2006). Using a 3D Finite Element (FE) model, (Shahraki et al. 2015) suggested a high rate of dynamic improvement at transition zone due to employment of the extra rails; a smoother transition was achieved with regard to abrupt change in the track stiffness. In fact, track's bending stiffness in the track was improved and the ballast layer demonstrated a reduction in the stress magnitudes.

(Esmaeili et al. 2020) investigated the effect of auxiliary rails on a ballasted track adjacent to a concrete culvert for different load velocities. Using FE model, the improvement in dynamic behavior was realized where the track accelerations and rail deflections were reduced. In another numerical study (Heydari-Noghabi, J. Varandas, et al. 2017), the efficiency of auxiliary rail was evaluated for the load passage from a slab track to a ballasted track[1]; smaller rail deflection was

---

[1]The vice versa direction is normally more detrimental (Sañudo et al. 2016).

demonstrated for both low and high load velocities. Moreover, considering complete width of the track, addition of two extra rails was suggested as an optimum number for this mitigation measure in transition zone.

The improvement in dynamic behavior of the track was also reported by (Chumyen et al. 2022), in which a 3D model was validated based on the findings of a field investigation (corresponding to the auxiliary rail) in (Heydari-Noghabi, Zakeri, et al. 2018). A better load distribution within the ballast layer was attributed to addition of two auxiliary rails. However, the soft track indicated a slight increase in displacement at the end of extra rail where its length is terminated. Furthermore, it was concluded that installing extra rails closer to the main rails results in a slightly better performance in dynamic response of the track.

3.2 Static stiffness

Considering the one-dimensional model in this thesis, extra rail, ER, is incorporated into the system simply by linear addition of its bending stiffness and mass to those of the beam element. Note that the ER's mechanical properties are equally considered as those of the main rail. Two configurations are investigated in this chapter; in the first case, ER is applied only to the soft track, while the system with ER in both soft and stiff tracks is considered as the second configuration. For the sake of brevity, mathematical derivation of the latter is neglected. Furthermore, the nominal track's mechanical model (defined in chapter 2) is accordingly modified for the corresponding analyses.

3.2.1 ODEs and static solutions

It is worthwhile to initially evaluate the effect of auxiliary rails on the *static stiffness* behavior at transition zone. Considering the first configuration, the static stiffness can be described through the ordinary differential equations, ODEs, of the system as follows.

$$w_1'''' + 4\gamma_1^4 w_1 = -F\delta(x - \overline{x}), \ \ 4\gamma_1^4 = k_1/nEI, \ n = 1,...4, \qquad x \leqslant x_{tp}, \quad (3.1a)$$

$$w_2'''' + 4\gamma_2^4 w_2 = -F\delta(x - \overline{x}), \ \ 4\gamma_2^4 = k_2/EI, \qquad\qquad\qquad x \geqslant x_{tp}, \quad (3.1b)$$

where the transition point is denoted by $x_{tp} = 0$; w_1 and w_2 indicate the static displacements at position x in the left ($x \leqslant x_{tp}$) and right ($x \geqslant x_{tp}$) domains, respectively; the Dirac delta function $\delta(x - \overline{x})$ signifies the position $\overline{x}$ at which the point load, F, is applied. Moreover, n is the coefficient corresponding to the

number of extra rails in the left domain (i.e. $n = 1$ signifies no ER, $n = 2$ signifies one ER, and so forth). Note that a maximum of three extra rails in half width of the track is considered for this study. In addition, numerical values of the system parameters are considered according to Table 2.1.

The ODEs in Equation 3.1 are of 4th order which in total require 8 boundary/interface conditions to be solved. Naturally, the general solution is superposition of the homogeneous and particular solutions. Note that before solving the Equation 3.1, for a better understanding, the homogeneous solution of the ODE's *generic* form is derived as follows. Substituting the trial solution $w = e^{\lambda x}$ in $w'''' + 4\gamma^4 w = 0$ and removing the common factor $e^{\lambda x}$, leads to the characteristic equation

$$\lambda^4 + 4\gamma^4 = 0 \qquad \rightarrow \qquad \lambda = \sqrt[4]{-1}\,\sqrt{2}\,\gamma. \tag{3.2}$$

Given the de Moivre's relation in Equation 2.13 and substituting all fourth roots of -1, $(\pm 1 \pm i)/\sqrt{2}$, in Equation 3.2, the corresponding roots read

$$\lambda_1 = \gamma(1 + i), \quad \lambda_2 = \gamma(1 - i), \quad \lambda_3 = \gamma(-1 + i), \quad \lambda_4 = \gamma(-1 - i). \tag{3.3}$$

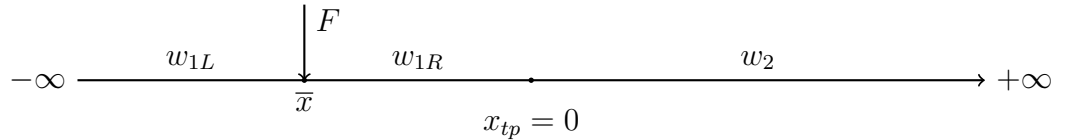The generic homogeneous solution, therefore, can be found as

$$w_h(x) = \sum_{m=1}^{4} C_m e^{\lambda_m x}, \qquad m = 1, \cdots, 4, \tag{3.4a}$$

$$w_h(x) = e^{\gamma x}\left(C_1 e^{\gamma i x} + C_2 e^{-\gamma i x}\right) + e^{-\gamma x}\left(C_3 e^{\gamma i x} + C_4 e^{-\gamma i x}\right), \tag{3.4b}$$

where the unknown constants C_m are determined through the boundary/interface conditions.

Turning back to the system's ODEs in Equation 3.1, it is simpler to derive the solutions by splitting each domain into two sub-domains due to presence of Dirac delta function. Thus, two load cases are considered as follows.

1. The load F is applied at $\overline{x} \leqslant 0$ in the left domain only.

The equations are therefore extended to three ODEs

$$
\begin{aligned}
w_{1L}'''' + 4\gamma_1^4 w_{1L} = 0, \quad w_{1R}'''' + 4\gamma_1^4 w_{1R} = 0, \qquad & x \leqslant x_{tp}, \\
w_2'''' + 4\gamma_2^4 w_2 = 0, \qquad\qquad\qquad\qquad\quad & x \geqslant x_{tp},
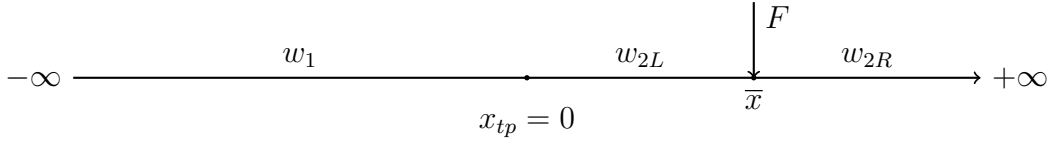\end{aligned}
\tag{3.5}
$$

with 12 interface/boundary conditions in total. Now considering the generic homogeneous solution in Equation 3.4b and applying 4 boundary conditions at infinite distance (zero displacement), the static solutions read[2]

$$
\begin{aligned}
w_{1L} &= e^{\gamma_1 x}(C_1 \cos(\gamma_1 x) + C_2 \sin(\gamma_1 x)), \\
w_{1R} &= e^{\gamma_1 x}(C_5 \cos(\gamma_1 x) + C_6 \sin(\gamma_1 x)) + e^{-\gamma_1 x}(C_7 \cos(\gamma_1 x) + C_8 \sin(\gamma_1 x)), \\
w_2 &= e^{-\gamma_2 x}(C_{11} \cos(\gamma_2 x) + C_{12} \sin(\gamma_2 x)).
\end{aligned}
$$

$$(3.6)$$

Furthermore, relations of the slope, bending moment, and shear force of the beam in the soft track are respectively defined as $\phi(x) = -w'$, $M(x) = -nEIw''$, and $V(x) = -nEIw'''$; same relations are considered for the stiff track, however, the factor n is ignored. By substituting Equation 3.6 into the following interface conditions at $\overline{x}$ and x_{tp}, the unknown constants in Equation 3.6 are derived to complete the system's static solutions[3].

$$
\begin{array}{ll}
w_{1L}(\overline{x}) = w_{1R}(\overline{x}), & w_{1R}(x_{tp}) = w_2(x_{tp}), \\
\phi_{1L}(\overline{x}) = \phi_{1R}(\overline{x}), & \phi_{1R}(x_{tp}) = \phi_2(x_{tp}), \\
M_{1R}(\overline{x}) = M_{1L}(\overline{x}), & M_{1R}(x_{tp}) = M_2(x_{tp}), \\
V_{1L}(\overline{x}) = F + V_{1R}(\overline{x}), & V_{1R}(x_{tp}) = V_2(x_{tp}).
\end{array}
$$

$$(3.7)$$

2. In the second load case, F is applied at $\overline{x} \geqslant 0$ in the right domain only.

So, the equations are extended to,

$$
\begin{aligned}
w_1'''' + 4\gamma_1^4 w_1 &= 0, & & x \leqslant x_{tp}, \\
w_{2L}'''' + 4\gamma_2^4 w_{2L} &= 0, \quad w_{2R}'''' + 4\gamma_2^4 w_{2R} = 0, & & x \geqslant x_{tp}.
\end{aligned}
$$

$$(3.8)$$

The static solutions of Equation 3.8 can be derived following the same procedures for the first load case. For the sake of brevity, the derivation, therefore, is not repeated.

The solutions corresponding to both load cases together describe the static displacement of the system with ER over soft track only. The solution corresponding to the second configuration (ER over all domains) can also be found through the aforementioned procedures.

---

[2]Note that $e^{\pm i\gamma x} = \cos\gamma x \pm i \sin\gamma x$ (Euler's formula).
[3]The term $F\delta(x - \overline{x})$ in Equation 3.1 is appeared through shear balance at the interface position $\overline{x}$.

3.2.2   Results and discussions

The effect of extra rails on the static response at transition zone is evaluated as follows. The static stiffness profiles ($F/w_{1L} = F/w_{1R}$ and $F/w_{2L} = F/w_{2R}$) are presented in Figure 3.1 and Figure 3.2 for the first and second configurations, respectively.
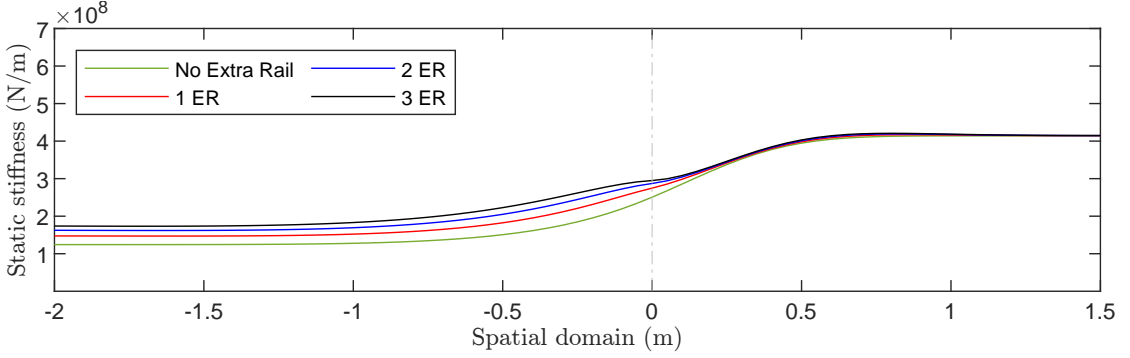

Figure 3.1: Static stiffness profile of the first configuration (extra rails, ERs, in the soft track only). The transition point $x_{tp} = 0$ is denoted by dash-dotted line.
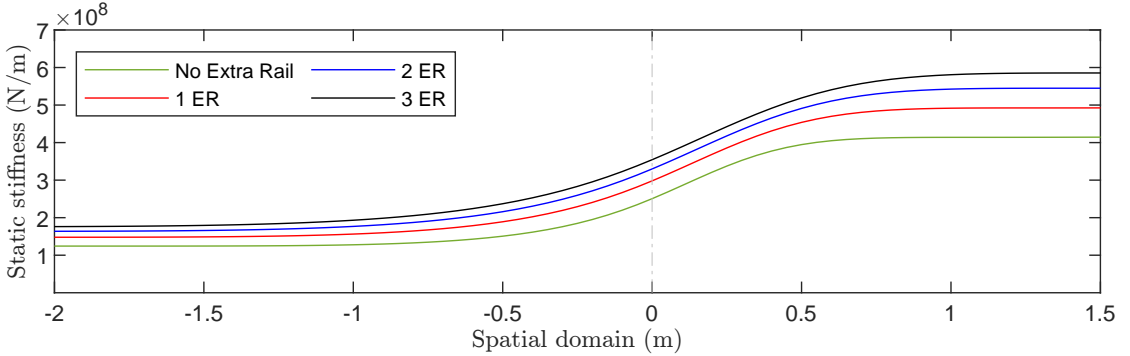

Figure 3.2: Static stiffness profile of the second configuration (extra rails, ERs, in both soft and stiff tracks). The transition point $x_{tp} = 0$ is denoted by dash-dotted line.

According to Figure 3.1, application of ER leads to a slight increase in static stiffness of the soft track, as expected. This increase in the stiff track is nil—except in the vicinity of transition point (x_{tp}). In contrast, the second configuration (Figure 3.2) indicates an almost uniform increase over all domain. That is, an upward shift without any noticeable change in the smoothness, as can be seen in Figure 3.2; the increase is more evident in the stiff track.

More importantly, the system with ER over left domain demonstrates a smoother

transition. This can be explained by smaller ratio of the right domain's static stiffness to that of the left domain in Figure 3.1.

Moreover, the improvement becomes less evident as the number of ER increases in both configurations. It should be noticed that these findings are valid only for load velocities that lead to a quasi-static response. Therefore, these results can not be associated to the system with a load moving, for example, with 70% of the critical velocity—in such case, dynamic stiffness should be addressed instead.

3.3 Dynamic analysis

In this section, the efficiency of extra rail is investigated through dynamic analysis at transition zone. Initially, the corresponding EOMs are derived through same procedures in chapter 2. Thereafter, the dynamical results corresponding to the aforementioned configurations are evaluated.

3.3.1 EOMs and dynamic solutions

Auxiliary rails are incorporated into the beam element via linear addition of EI by the factor n, as discussed in section 3.2. Moreover, the linear mass of the beam element is defined as

$$\bar{\rho} = n\rho + \rho_s,$$

where ρ is linear mass of the rail (either the additional or the original rail). ρ_s is half of the sleeper mass (250/2 kg) which is distributed over the distance between two sleepers ($s_{sb} = 0.6$ m); that is, $\rho_s = 125/0.6 = 208.33$ kg/m. Clearly, addition of rail has no effect on the system damping.

Thus, the EOMs of the system corresponding to the first configuration are derived as

$$nEIw_1'''' + \bar{\rho}\ddot{w}_1 + c_1\dot{w}_1 + k_1w_1 = -F\delta(x - vt), \qquad\qquad x \leqslant x_{tp}, \qquad (3.9)$$

$$EIw_2'''' + \rho\ddot{w}_2 + c_2\dot{w}_2 + k_2w_2 = -F\delta(x - vt), \qquad\qquad x \geqslant x_{tp}, \qquad (3.10)$$

where all other parameters are equivalently explained as in chapter 2. In addition, the boundary and interface conditions (notice the appearance of factor n corresponding to number of ERs) read

$$\lim_{(x-vt)\to-\infty} w_1(x,t) = 0, \qquad\qquad \lim_{(x-vt)\to+\infty} w_2(x,t) = 0, \qquad\qquad (3.11)$$

$$w_1(x_{tp}, t) = w_2(x_{tp}, t), \qquad\qquad nw_1^{''}(x_{tp}, t) = w_2^{''}(x_{tp}, t), \qquad (3.12a)$$

$$w_1^{'}(x_{tp}, t) = w_2^{'}(x_{tp}, t), \qquad\qquad nw_1^{'''}(x_{tp}, t) = w_2^{'''}(x_{tp}, t). \qquad (3.12b)$$

Applying Fourier transforms to Equation 3.9 over time gives

$$\widetilde{w}_1^{''''} - \beta_1^4 \widetilde{w}_1 = -\frac{Fe^{i\omega x/v}}{vnEI}, \quad \beta_1^4 = (\bar{\rho}\omega^2 - ic_1\omega - k_1)/nEI, \ x \leqslant x_{tp}, \quad (3.13a)$$

$$\widetilde{w}_2^{''''} - \beta_2^4 \widetilde{w}_2 = -\frac{Fe^{i\omega x/v}}{vEI}, \quad \beta_2^4 = (\rho\omega^2 - ic_2\omega - k_2)/EI, \quad x \geqslant x_{tp}. \quad (3.13b)$$

Applying boundary conditions at infinite distance and superimposing the homogeneous and particular solutions of Equation 3.13 leads to the general solution in Fourier domain as

$$\widetilde{w}_1(x, \omega) = A_1 e^{\beta_1 x} + A_2 e^{i\beta_1 x} + \frac{-Fv^3 e^{-i\omega x/v}}{nEI(\omega^4 - \beta_1^4 v^4)}, \qquad\qquad x \leqslant x_{tp}, \qquad (3.14a)$$

$$\widetilde{w}_2(x, \omega) = B_3 e^{\beta_2 x} + B_4 e^{i\beta_2 x} + \frac{-Fv^3 e^{-i\omega x/v}}{EI(\omega^4 - \beta_2^4 v^4)}, \qquad\qquad x \geqslant x_{tp}, \qquad (3.14b)$$

where the unknown constants can be found through Equation 3.12 in their Fourier domain. Eventually, after applying the inverse Fourier transform, the time domain solutions are numerically derived. Accordingly, the solutions of the second configuration (ER over all domains) can be found.

3.3.2 Results and discussions

Dynamic amplification factor

The efficiency of additional rails in mitigating the amplified response can be evaluated through dynamic amplification factor, DAF. As defined in (Equation 2.27), the DAF is the ratio of maximum transient displacement to the maximum displacement in the steady state regime of the same system at a specified load velocity.

The DAF corresponding to both configurations are presented in Figure 3.3. Clearly, addition of extra rail leads to improvement in the amplified response through shifting the critical velocity to a higher value. That is, the response at the same load velocity v, decreases with increasing number of ER. This explains the mechanism corresponding to this mitigation measure.

In the first configuration (ER over soft track; dashed curves), the peaks demonstrate increase in amplitude compared to both nominal track and second configuration (ER over all domains; solid curves). This can be explained by inhomogeneity in bending stiffness and mass due to discontinuity of ER at transition point, x_{tp}. Naturally, this inhomogeneity is more evident for larger number of ER. Moreover, the aforementioned behaviors in both configurations demonstrate a smaller rate of change for larger number of ER compared to when only one ER is added; this reinforces the findings in (Heydari-Noghabi, J. Varandas, et al. 2017)[4].
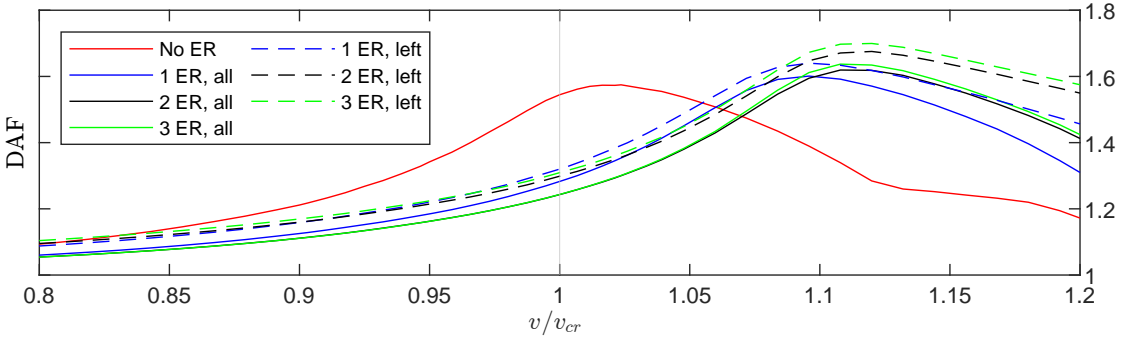

Figure 3.3: Dynamic amplification factor, DAF, of the system with and without extra rails, ERs. Dashed curves are correspondent to the system with ER only over soft track (first configuration). Solid curves are correspondent to the system with ER over both soft and stiff tracks (second configuration). The nominal track is denoted by red curve. v_{cr} is critical velocity in the nominal track.

Power input

As discussed in subsection 2.4.6, ratio of the maximum transient power input to the steady-state power input provides an indirect benchmark to assess the damage in the foundation due to the load passage at transition zone.

Power inputs of the aforementioned configurations are presented in Figure 3.4 for same relative velocity (95% *of the critical velocity in each corresponding system*). Compared to the nominal track, both configurations demonstrate reduction in the steady-state and transient power inputs in the soft domain. However, the employment of ER leads to a slight increase in power input ratio resulting in larger potential damage to the supporting structure (indirectly), compared to the nominal track. Note that this undesired behavior is more evident in the first configuration compared to the second one.

---

[4]Note that in the aforementioned study complete width of the track has been considered.
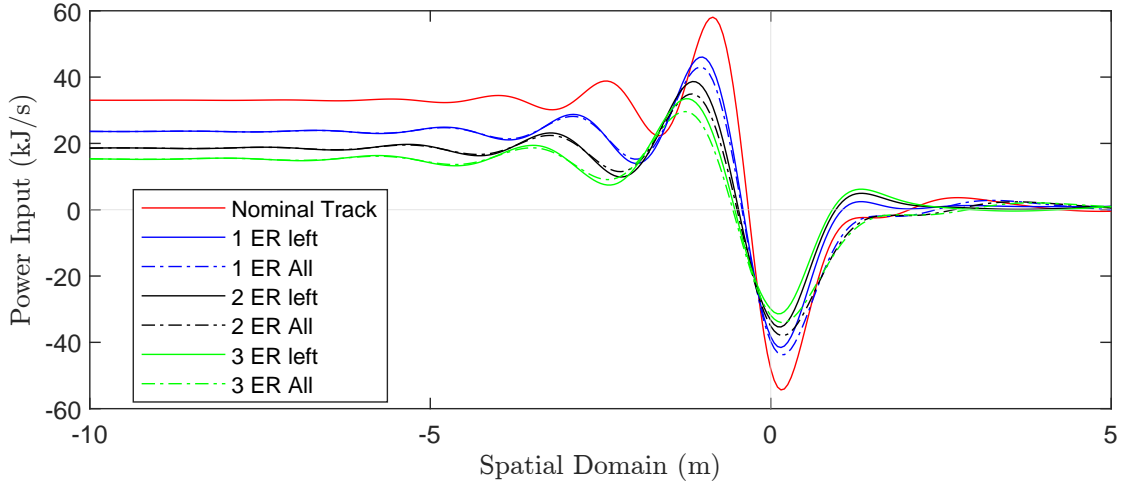
Figure 3.4: Power input of the first (ER over left domain; solid curves) and the second (ER over all domains; dashed curves) configurations. Transition point is $x_{tp} = 0$. Load velocity is 95% of critical velocity in each corresponding system.
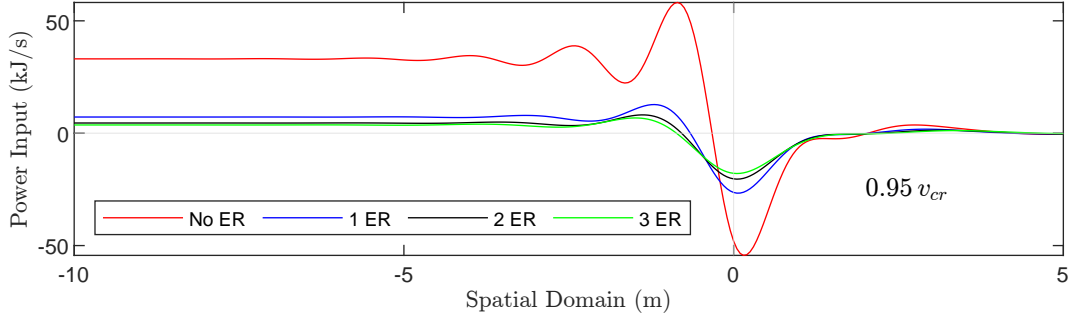

Figure 3.5: Power input of the second configuration (ER in all domains). Transition point is $x_{tp} = 0$. The relative velocity is 95% of the critical velocity corresponding to the nominal track.

On the other hand, when the systems are considered at a lower relative velocity (95% *of the critical velocity corresponding to the nominal track*), addition of rail significantly reduces the power input amplification compared to the nominal track, as can be seen in Figure 3.5 (not shown for the first configuration). Moreover, the power input demonstrates a smoother energy exchange between the track and the load in the vicinity of transition point. This leads to a better load distribution over larger areas along the transition zone.

To sum up, considering the same relative velocity (load velocity relative to *the critical velocity in the corresponding system*), the amplification in power input is very similar in the systems with and without ER (i.e., the amplification is not reduced by adding the ER). This points to the fact that the amplification reduction mechanism in the system with ER, at lower relative velocity, is the shifting of the critical velocity to higher values.

Chapter 4

Under Sleeper Pad

Under sleeper pad, USP, is a viscoelastic material that is attached to the bottom surface of the sleepers. USP can decrease the contact pressure between the sleepers and the ballast layer. The application of USP normally modifies the track stiffness and improves the correspondent load distribution. After a literature review, the efficiency of USP in improving the transition zone's behavior is evaluated semi-analytically and numerically (FEM). Then, USP's serial incorporation into the one-dimensional system is briefly discussed. Accordingly, a limit case is derived such that the system behaves exactly as in the steady-state regime, despite abrupt change in the profile stiffness of the track. In addition, multiple arrangements of USPs along the track with sinusoidal variation in stiffness are investigated for various transition lengths. Finally, it is concluded that the efficiency of this mitigation measure is significantly dependent on their resiliency and arrangement, as well as the track's stiffness variation; improper design of USPs alignment can adversely result in even more amplified responses.

4.1   Literature review

Few studies have evaluated the influence of USPs at transition zones. For example, (Insa, Salvador, Inarejos, and Roda 2012) found that the employment of USPs along the transition region can decrease the stiffness variation and improve the dynamic wheel-rail interactions; this holds for train velocities of about 300 km/h. In another study, (Insa, Salvador, Inarejos, and Medina 2014) numerically investigated a 3D model, in which USPs at different installing locations were considered; namely along the whole domains and at the stiff track only (with and without transition zone). It was concluded that applying USP hardly has any impact on the track components below the ballast layer in terms of their displacements and stresses.

(Paixão, Alves Ribeiro, et al. 2015) carried out a field investigation of transition regions with concrete culverts. The track was modified by applying exclusively soft USP that covers about half of the transition length and whole domain of the stiff track. Their findings illustrate that the track stiffness was significantly reduced while displacements and accelerations of the rails and the sleepers were amplified. Afterward, mechanical model of the same track was numerically analyzed in 2D by (Alves Ribeiro et al. 2015), in which gradual increase of the USPs' resiliency along the transition zone was proposed to improve the track behavior.

Over two years, (Mottahed et al. 2019) experimentally investigated the influence of USPs with three different arrangements on ballasted transition zones and their encountered ballasted bridge (two-span). Various train speeds were consid-

ered, while one type of USP was adopted throughout the investigation. Base data corresponding to the acceleration and deflection were recorded for the original track as the 1st configuration. Then, new USP-integrated sleepers were installed only at the bridge section as the 2nd configuration. And in case 3, transition regions were modified too. Findings regarding the first span of the bridge are as follows. When comparing the 2nd configuration to the original track, average of the rails accelerations, and average max. accelerations of the sleepers and bridge deck were reduced by 34%, 11%, and 32%, respectively. This reduction for the latter was 66% when USPs were applied over all domains. However, the rails and sleepers accelerations were increased for some speeds in the range of 40-60 km/h. Furthermore, average displacement of the bridge deck was reduced by 19% and 20% for cases 2 and 3, respectively. Finally, this field investigation concludes that in general, the application of USPs results in improving vibration behavior of the bridge.

In another numerical and experimental investigation in Portuguese railway, the influence of USPs on transition zone was studied by (Paixão, Fortunato, et al. 2014); with maximum train speed of about 220 km/h. In the experimental work, USPs with two different bedding moduli were respectively applied along the transition region (120 MN/m^3) and along a short distant before and over the bridge (130 MN/m^3). Additionally, an optimized arrangement of USPs was presented with reference to the numerical analysis, in which the same field was modeled and calibrated in 3D through finite element method. The optimum alignment includes very stiff USPs for a few sleepers located in the beginning of transition zone and continued by softer USPs up until the onset of the stiff track, after which it continued by even softer USPs over the stiff domain. It was led to a smoother stiffness variation. This study demonstrates that applying USPs decreases the transferred loads and transmitted vibrations to the ballast layer. Furthermore, it was suggested to apply USPs along all corresponding domains or economically only at the transition zones with careful design, as USP might change the vertical stiffness negatively.

In all, the previous studies illustrate an overall efficiency of USPs in improving the track behavior. While the inefficiency of USPs are normally attributed to the improper arrangement of USPs along the track. Finally, the influence of USPs on the nominal track (defined in chapter 2) is evaluated in the next section.

4.2   Serial coupling of USPs

To be incorporated into the one-dimensional train-track system, USP can be modeled as a linear spring (k_{usp}) and a dash-pot (c_{usp}), which are respectively coupled in series to k_j and c_j of the foundation. Therefore, the equivalent stiffness and the equivalent damping of the track simply is derived as

$$k_{j,eq} = \frac{1}{k_j^{-1} + k_{\mathrm{usp}}^{-1}}, \qquad c_{j,eq} = \frac{1}{c_j^{-1} + c_{\mathrm{usp}}^{-1}}, \tag{4.1}$$

where $c_j = 2\zeta_j \sqrt{k_j \rho}$, and $c_{\mathrm{usp}} = 2\zeta_{\mathrm{usp}} \sqrt{k_{\mathrm{usp}} \rho_{\mathrm{usp}}}$; ρ_{usp} is linear mass of the USP[1].

Clearly, in this model, the incorporation of under sleeper pads leads to reduction in equivalent stiffness of the track. This is due to the mathematical definition of the springs being coupled in series. To clarify, consider a system, in which a spring with constant unit stiffness (K_1) is serially coupled to another spring (K_2) which varies in magnitude, Figure 4.1. As it can be seen, it is impossible for the system's equivalent stiffness to be stiffer than each of the springs individually. In an extreme case, the maximum equivalent stiffness is equal to K_1 when K_2 tends to infinity, meaning K_2 can be simply ignored from the model[2]. Therefore, applying USP exclusively in the nominal soft track should be avoided as its equivalent stiffness becomes even more softer which eventually leads to stronger vibrations. This in turn limits the application of USPs to the stiff track only.
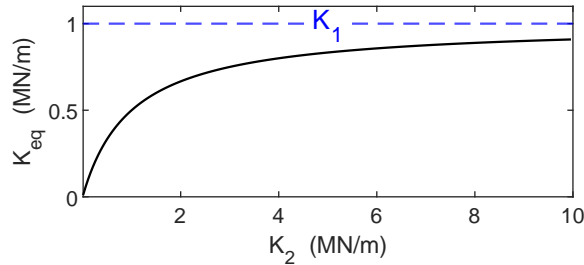

Figure 4.1: Serial coupling of two springs. $K_1 = 1$ MN/m; K_2 varies; black curve denotes K_{eq}.

Magnitudes of the mechanical properties can be found in the study by (Johansson et al. 2008)[3] which is presented in Table 4.1; damping values are distributed

---

[1] $\rho_{\mathrm{usp}} = \rho_{\mathrm{vm}} A_{\mathrm{eff}} t_{\mathrm{usp}} / s_{sb}$, where ρ_{vm} is the volumetric mass density of USP; A_{eff} is the effective area of the sleeper's bottom surface (≈ 0.24 m^2); t_{usp} is the thickness of USP; and s_{sb} is the sleeper bay spacing as in Table 2.1.

[2] Similar to the sleepers which are too stiff to be considered in the equivalent stiffness of the track, as in subsection 2.2.1

[3] The adopted parameters in that article are based on their coordination with Getzner Werkstoffe GmbH in the industry.

($s_{sb} = 0.6$ m) for the current work; the volumetric mass density of USP is 500 kg/m^3.

<p style="text-align:center">Table 4.1: Mechanical Properties of USPs</p>

USP Type	Soft	Moderate	Stiff
Bedding Modulus, N/mm^3	0.1	0.2	0.3
Static Stiffness, MN/m	35	70	105
Damping, Ns/m/m	4091	11575	17441

Accordingly, serial coupling of *moderate* USP to the stiff track ($k_2 = 250$ MN/m) results in $k_{2,eq} = 54.69$ MN/m; the modified stiffness ratio is now 1.09, meaning the amplified response is almost completely suppressed. On the other hand, integrating *soft* USPs into the soft track ($k_1 = 50$ MN/m) increases the stiffness ratio from 5 to 12.1. Therefore, in the context of USP efficiency, not only are their stiffness magnitude of high importance, but also their installing locations according to the stiffness profile of the track. Neglecting these factors might intensify the already amplified vibrations even more.

4.3   A limit case

Consider the stiffness profile of the track with an abrupt jump, in which USPs are serially coupled to the stiff track only. The stiffness and damping ratio of the USPs can be derived as a limit case such that the equivalent stiffness of the track becomes completely homogeneous along the spatial domain. Equating the soft track's stiffness and damping to those of the stiff track with USPs, readily results in the limit case as follows.

$$k_1 = k_{2,eq} = \frac{k_2\, k_{usp}}{k_2 + k_{usp}} \qquad \rightarrow \qquad k_{usp} = \frac{s_r k_1}{s_r - 1}, \tag{4.2a}$$

$$c_1 = c_{2,eq} = \frac{c_2\, c_{usp}}{c_2 + c_{usp}} \qquad \rightarrow \qquad \zeta_{usp} = \frac{c_1}{2\sqrt{k_{usp}\rho_{usp}}(1 - c_1/c_2)}, \tag{4.2b}$$

where $s_r = k_2/k_1$ is the stiffness ratio (Table 2.1).

Assume $\rho_{usp} = 4$ kg/m, and consider $s_{sb} = 0.6$ m, $s_r = 5$, $k_1 = 50/0.6$ MN/m^2, and $\zeta_1 = \zeta_2 = 0.05$, as before. Given that, Equation 4.2 results in $k_{usp} = 62.5/0.6$ MN/m^2 and $\zeta_{usp} = 0.663$. That is, theoretically speaking, the application of such USPs at the stiff track leads to a system that behaves exactly as

in the steady-state regime without any transition radiation—despite the nominal stiffness ratio being as high as 5. Note that this ideal result can be attributed to the *simplified* model of the train-track system.

4.4   Smooth variation in stiffness

To further study the effect of USPs' arrangement (installing locations) on the track behavior, different transition lengths are considered in this section. In doing so, numerical simulations (FEM) are performed for sinusoidal variation in the stiffness profile at transition zone based on the one-dimensional model in (Fărăgău, Andrei V Metrikine, et al. 2019)[4]

Note that for larger transition lengths, the application of USP is unnecessary; since the smooth sinusoidal variation in the stiffness profile can be already a mitigation measure by itself (e.g. 9 m transition length). However, the amplifications possibly can be improved for smaller transition lengths (e.g. 3 m) through applying USP.

Before performing the simulations, it is worthy to compare the stiffness profile of the track with and without USP for different transition lengths, as can be seen in Figure 4.2. Consider the transition length with 6 m; applying USP only in the stiff track results in losing the smooth variation in profile, which is not true for 0.1 m transition length. Therefore, advance perception of the stiffness profile lays the basis for an efficient alignment along the track when integrating USPs into the system.
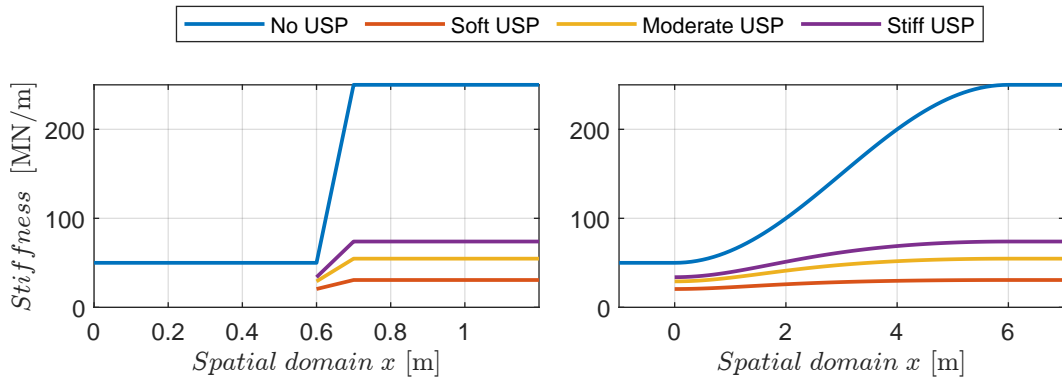

Figure 4.2: Stiffness profile of the track with and without USP for transition lengths 0.1 m (left panel) and 6 m (right panel). The latter is sinusoidally smooth.

---

[4]The authors of this article are mentors of the current thesis. MATLAB codes were provided for simulations in this chapter; all credit goes to Ir. Andrei B. Fărăgău. To incorporate the USP into the model, the codes were slightly modified.

4.4.1 USP arrangement

To evaluate dynamic response corresponding to USP, three arrangements with different transition lengths are considered in (Table 4.2). Notice that the process of aligning is correspondent to gap removal of the stiffness between the non-modified and USP-integrated tracks in Figure 4.2. Arrangement nicety is the least in case 1 and is gradually increased for its successors with the case 3 being the most optimum. The aim is to sufficiently illustrate the optimization trend. Subsequently, all corresponding results are presented and discussed in the next section.

Table 4.2: Arrangement of USPs along the track; x_s, x_q, and x_{tc} are the onset, a quarter, and center of the transition zone, respectively. $x > x_{tc}$ covers the stiff track too. For USP types, see Table 4.1.

	USP Stiffness			Transition Lengths, m
	$x_s < x < x_q$	$x_q < x < x_{tc}$	$x > x_{tc}$	
Case 1	same type	same type	same type	0.1, 3, 6
Case 2	–	–	soft/moderate/stiff	0.1, 3, 6
Case 3	–	stiff	moderate	3, 6

4.5 Results and discussions

As discussed in chapter 2, power input can be indirectly attributed to the damage in foundation. Therefore, the utmost goal is to achieve the enhanced efficiency through an alignment whose power input amplification demonstrates reduction. Accordingly, the analyses layout is started by the least subtle alignments, mainly with regard to the power input plots, and is developed into an optimized configuration for which the corresponding DAF is also addressed.

The power inputs in case 1 and 2 are presented in Figure 4.3. As the transition length becomes larger, the system without USP benefits from a smoother and smaller energy input, as expected. In contrast, for transition length 0.1 m, both cases experience a behavior similar to the steady-state response in the event of applying moderate USP. In case 1 (USPs over $x > x_s$), the ratio of peak to the steady-state power input in the left domain indicates an increase for longer transition and softer USPs, which is not desired. Moreover, power inputs in case 2 (USP over $x > x_{tc}$) demonstrate a smoother transition as the amount of energy back to the external force from the track is reduced in the vicinity of transition
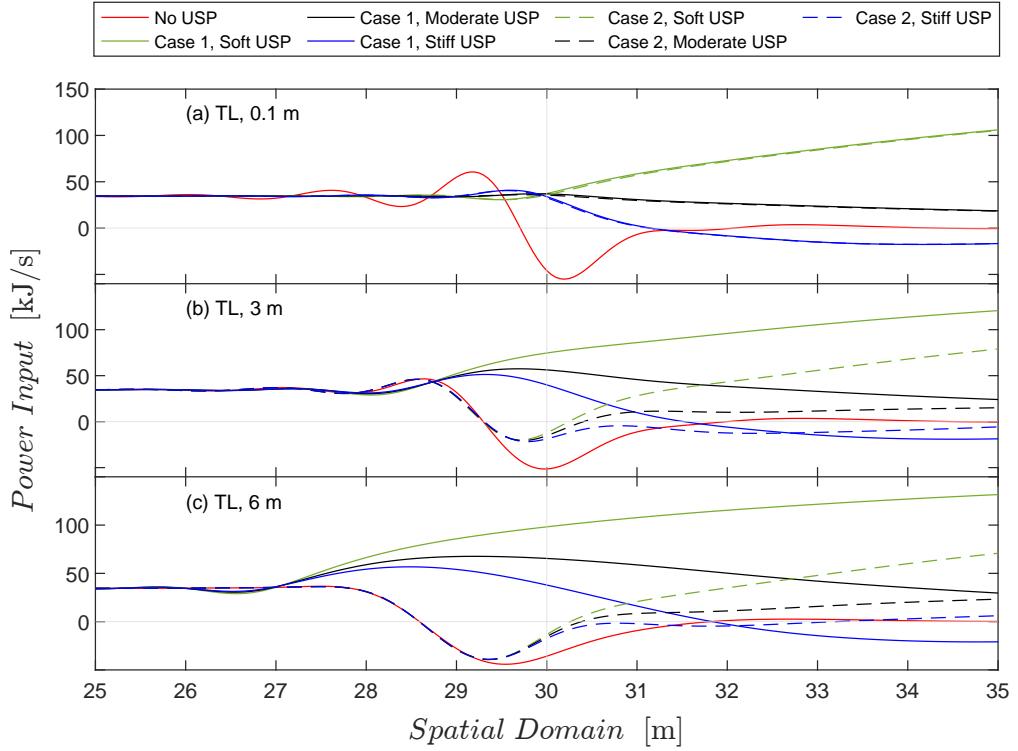
Figure 4.3: Power input corresponding to the USP arrangements in Case 1 (USP over $x > x_s$) and Case 2 (USP over $x > x_{tc}$) for different transition lengths. $x_{tp} = 30$ m is position of transition center; load velocity is 0.95% of critical velocity corresponding to the system without USP; TL denotes transition length

point. Naturally, this leads to truncating the peak in case 1 while keeping the smoothness in case 2 through an optimum arrangement, case 3, as can be seen in Figure 4.4. This improvement for transition length 6 m, however, is limited to removing the trough only (negative power input). Consider the transition length 3 m; the ratio of the peak to the steady state power input is reduced in the optimum alignment leading to less damage in the foundation compared to the system without USP.

Displacements of the optimum configuration (3 m) at different time-moments are presented in Figure 4.5. The eigenfield in the system with USP almost demonstrates a steady-state response where hardly any free field radiation can be signified (last panel).

Moreover, the correspondent dynamic amplification factor, DAF[5], is presented in Figure 4.6. Clearly, applying USPs with an optimized arrangement can significantly improve the amplified response at transition zone. The DAF corresponding
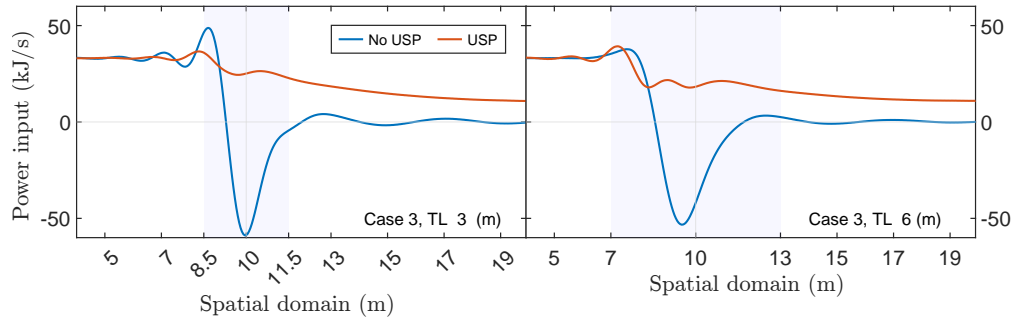
---

[5]Defined in chapter 2

Figure 4.4: Power input of the system corresponding to the optimum arrangement of USPs, Cases 3. $x_{tp} = 10$ m is transition point; load velocity is 0.95% of critical velocity corresponding to the system without USP; TL denotes transition length
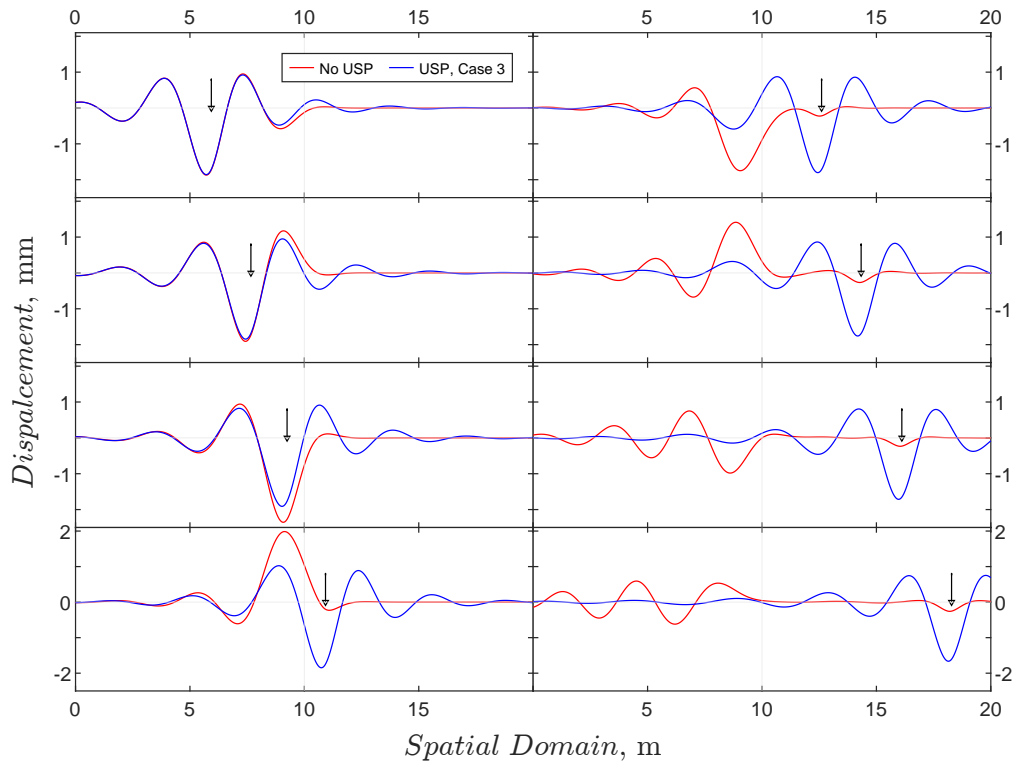

Figure 4.5: Snapshots of displacement fields at different time-moments corresponding to the systems without USP (red curve) and with optimum arrangement of USPs (blue); see in the order of top left panel downward and then top right panel downward. Transition length is $l_t = 3$ m; transition point is $x_{tp} = 10$ m; load velocity is 0.95% of critical velocity corresponding to the system without USP.
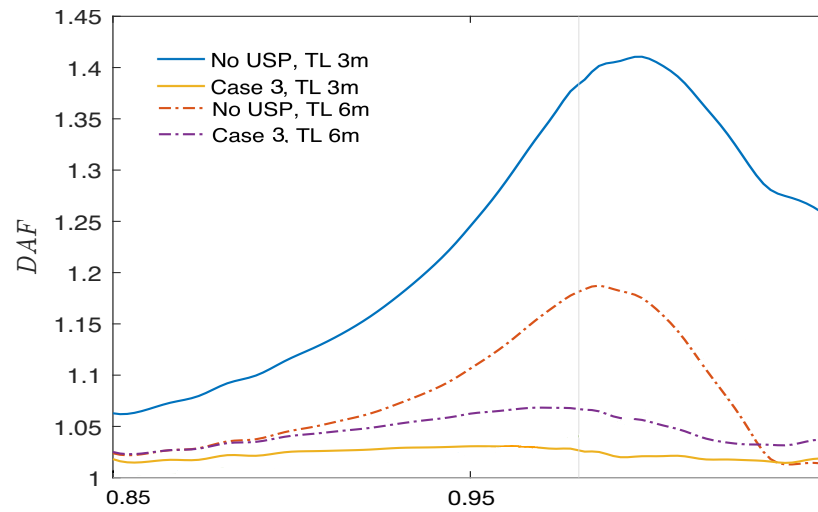
Figure 4.6: DAF of the optimum configuration vs relative velocity (v/v_{cr}); v_{cr} is critical velocity corresponding to the system without USP. TL stands for transition length.

to the system with 3 m transition length indicates an almost completely flattened curve.

Chapter 5

Conclusions

5.1   TMD

The feasibility of applying TMD for controlling the amplified vibrations at transition zone was studied as the main goal of the thesis. In response to the first research question, the conclusions corresponding to the efficiency of TMD mitigation measure are presented as follows.

- The optimized values of the TMD's parameters in the soft track seems to be realistic which suggest the possible feasibility of their application in practice for further studies.

- Considering the dispersion analysis, applying the optimized TMD results in new stop bands in the system. The frequencies within the stop band in the optimized soft track covers the tuned frequency (and its neighboring frequencies) for which the objective functions in the optimization problem were minimized (the discrepancy between the soft and the stiff tracks' wavenumbers). However, the system demonstrates free propagating wave behind the load, regardless of the load velocity (except at zero).

- Addition of TMD leads to significant reduction in DAF amplitude at load velocity for which the system was optimized. In fact, the DAF peak (critical velocity) shifts toward a lower relative velocity. This mechanism results in the optimized system at supercritical regime. This behavior, however, is undesired and should be avoided.

- The TMD application leads to noticeable reduction in Fourier displacement at the tuned frequency. The Fourier peak demonstrates a shift from the tuned frequency to that of the free propagating wave behind the load in the steady-state regime.

- Addition of TMD leads to significant reduction in ratio of the maximum transient power input to the steady-state power input, as an indirect benchmark, which results in less potential damage to the supporting structure.

- Applying TMD can significantly decrease both energy flux and spectral energy density corresponding to the leftward free field radiation at velocity/frequency for which the vibration absorbers were optimized. This might be attributed to large damping in the TMD, strong counteractive forces between the TMD and the beam, and possibly the energy trap at transition zone.

To sum up, the employment of tuned mass damper can improve the dynamical performance corresponding to transition zone. This mitigation measure, however, is more evident for frequency/load velocity at which the TMDs are optimized.

5.2   Auxiliary rail

In response to the second research question, application of auxiliary rails at transition zone was investigated for two configurations (extra rail, ER, over soft track, and ER over all domains). Moreover, different number of ER were considered for both static and dynamic analyses. Conclusions are established as follows.

- Addition of ER over soft track leads to smoother static stiffness compared to addition of ER over all domains. Results corresponding to static stiffness can only be attributed to load velocities that lead to a quasi-static response.

- At velocities relative to the critical velocities in each corresponding system, the DAF results will either not change noticeably (ER over both domains) or increase (ER over soft track). Since the critical velocity shifts to higher values, the response at the same load velocity v, decreases with increasing number of ER. Addition of ER over soft track leads to inhomogeneity in bending stiffness and mass at transition point. This explains the larger DAF compared to the configuration with ER over all domains.

- Considering the same relative velocity (load velocity relative to the critical velocity in the corresponding system), addition of ER results in slightly larger (potential) damage to the foundation. As power input ratio is narrowly increased for both configurations compared to the nominal track. In contrast, the amplification was significantly decreased at the same load speed (i.e. $v = 95\%v_{cr}$; related to the critical velocity in nominal track).

To sum up, two mechanisms can be mainly attributed to improvement in the amplified response at transition zone, due to application of auxiliary rail. First, the smaller power input and dynamic amplification factor is due to the shift in critical velocity. Second, additional rail leads to a better load distribution over a larger area.

5.3 USP

The efficiency of USP in reducing the amplified vibrations at transition zone was studied in response to the third research question. Multiple arrangements of USPs were simulated for the system with sinusoidal variation in stiffness. The investigation based on the one-dimensional model is concluded as follows.

- A limiting case corresponding to the USP employment was recognized, in which the piece-wise homogeneous system was modified to a system that entirely represents the steady-state behavior. The limitation corresponding to the simplified mechanical model should not be underestimated in obtaining such favorable result.

- USP can significantly affect the stiffness profile of the track; due to serial integration with foundation, addition of USP alone can not make the track stiffer.

- USP efficiency is strongly dependent on their types, arrangement, and the stiffness variation of the track. As a result, advance perception of the latter plays an essential role in designing a safe and efficient mitigation measure. Otherwise, the employment of USP might lead to an even more amplified response. Clearly, a mitigation design with USP is unique and no particular arrangement can be recommended for other transition zones.

Appendix A

A.1 Spectral energy density

To consider the *spectral energy density* in Fourier domain, Equation 2.30 is reformulated in terms of frequency as follows (Van Dalen et al. 2015). Let $\tilde{v} = i\omega\tilde{w}$ be the beam velocity, and

$$w = \frac{1}{2\pi} \int_{-\infty}^{\infty} \widetilde{w} e^{i\omega t} \, \mathrm{d}\omega. \tag{A.1}$$

Using the auxiliary variable $\overline{\omega}$ for the beam velocity and substituting all corresponding Fourier-domain terms in the Equation 2.30,

$$E_f(x) = \frac{\pm EI}{4\pi^2} \int\limits_{-\infty}^{\infty} \int\limits_{-\infty}^{\infty} \int\limits_{-\infty}^{\infty} \left(\widetilde{w}_f'''(\omega)\tilde{v}_f(\overline{\omega}) - \widetilde{w}_f''(\omega)\tilde{v}_f'(\overline{\omega}) \right) e^{i\,(\omega + \overline{\omega})\,t} \, \mathrm{d}\overline{\omega}\,\mathrm{d}\omega\,\mathrm{d}t, \tag{A.2}$$

where

$$\int\limits_{-\infty}^{\infty} e^{i\,(\omega + \overline{\omega})\,t} \, \mathrm{d}t = 2\pi\delta(\omega + \overline{\omega}), \tag{A.3}$$

and

$$E_f(x) = \frac{\pm EI}{2\pi} \int\limits_{-\infty}^{\infty} \int\limits_{-\infty}^{\infty} \left(\widetilde{w}_f'''(\omega)\tilde{v}_f(\overline{\omega}) - \widetilde{w}_f''(\omega)\tilde{v}_f'(\overline{\omega}) \right) \delta(\omega + \overline{\omega}) \, \mathrm{d}\overline{\omega}\,\mathrm{d}\omega. \tag{A.4}$$

Considering Equation 2.5b,

$$\int\limits_{-\infty}^{\infty} \tilde{v}_f(\overline{\omega})\, \delta(\overline{\omega} - (-\omega))\, \mathrm{d}\overline{\omega} = \tilde{v}_f(-\omega), \tag{A.5}$$

$$E_f(x) = \frac{\pm EI}{2\pi} \int\limits_{-\infty}^{\infty} \widetilde{w}_f'''(\omega)\tilde{v}_f(-\omega) - \widetilde{w}_f''(\omega)\tilde{v}_f'(-\omega)\, \mathrm{d}\omega. \tag{A.6}$$

Since the factors in the integrand are real-valued in their space-time domain, their Fourier transforms are conjugate symmetric; $\tilde{v}_f(-\omega) = \tilde{v}_f^*(\omega)$. Therefore,

$$E_f(x) = \frac{\pm EI}{2\pi} \int\limits_{-\infty}^{\infty} \widetilde{w}_f'''(\omega)\tilde{v}_f^*(\omega) - \widetilde{w}_f''(\omega)\tilde{v}_f^{*'}(\omega)\, \mathrm{d}\omega. \tag{A.7}$$

The conjugate symmetry property makes the real part of the Fourier transform to be *even*, hence symmetric with respect to the vertical axis. That is, $E_f(x)$ in the last equation is equivalent to two times of the same integral but with zero lower bound, $\{\omega \in \mathbb{R} \,|\, 0 \leqslant \omega < -\infty\}$. Finally, given a particular cross-section of the beam, the energy flux of the free-field reads

$$E_f(x) = \frac{\pm EI}{\pi} \int\limits_{0}^{\infty} \mathrm{Re}\{\widetilde{w}_f'''\tilde{v}_f^* - \widetilde{w}_f''\tilde{v}_f^{*'}\}\, \mathrm{d}\omega. \tag{A.8}$$

Bibliography

Alves Ribeiro, Cristina, André Paixão, Eduardo Fortunato, and Rui Calçada (2015). "Under sleeper pads in transition zones at railway underpasses: numerical modelling and experimental validation". In: *Structure and Infrastructure Engineering* 11.11, pp. 1432–1449.

Boas, M.L. (2006). *Mathematical Methods in the Physical Sciences*. Wiley. ISBN: 9780471365808. URL: https://books.google.nl/books?id=lgJOQgAACAAJ.

Chumyen, P, DP Connolly, PK Woodward, and V Markine (2022). "The effect of soil improvement and auxiliary rails at railway track transition zones". In: *Soil Dynamics and Earthquake Engineering* 155, p. 107200.

Dahlberg, Tore (2010). "Railway track stiffness variations–consequences and countermeasures". In: *International journal of civil engineering* 8.1, pp. 1–12.

Deb, K, Amrit Pratap, Sameer Agarwal, and TAMT Meyarivan (2002). "A fast and elitist multiobjective genetic algorithm: NSGA-II". In: *IEEE transactions on evolutionary computation* 6.2, pp. 182–197.

Den Hartog, Jacob Pieter (1985). *Mechanical vibrations*. Courier Corporation.

Dieterman, HA, V Metrikine, et al. (1997). "Steady-state displacements of a beam on an elastic half-space due to a uniformly moving constant load". In: *European Journal of Mechanics Series A Solids* 16, pp. 295–306.

Eiberg, Hans, Jesper Troelsen, Mette Nielsen, Annemette Mikkelsen, Jonas Mengel-From, Klaus W Kjaer, and Lars Hansen (2008). "Blue eye color in humans may be caused by a perfectly associated founder mutation in a regulatory element located within the HERC2 gene inhibiting OCA2 expression". In: *Human genetics* 123.2, pp. 177–187.

Elias, Said and Vasant Matsagar (2017). "Research developments in vibration control of structures using passive tuned mass dampers". In: *Annual Reviews in Control* 44, pp. 129–156.

Esmaeili, Morteza, Hamidreza Heydari-Noghabi, and Mehdi Kamali (2020). "Numerical investigation of railway transition zones stiffened with auxiliary rails". In: *Proceedings of the institution of civil engineers-transport*. Vol. 173. 5. Thomas Telford Ltd, pp. 299–308.

61

Esmailzadeh, E. and N. Jalili (Oct. 1998). "Optimum Design of Vibration Absorbers for Structurally Damped Timoshenko Beams". In: *Journal of Vibration and Acoustics* 120.4, pp. 833–841. ISSN: 1048-9002. URL: https://doi.org/10.1115/1.2893908.

Fara, Andrea (2014). "Transition zones for railway bridges: a study of the Sikån bridge". MA thesis. Luleå, Sweden: Luleå University of Technology.

Faragau, Andrei (2017). "Transition radiation in an inhomogeneous and non-linear one-dimensional system". MA thesis. Delft, The Netherlands: Delft University of Technology. URL: http://resolver.tudelft.nl/uuid:faa618c3-260b-4bfb-919c-d56a215bd0c7.

Fărăgău, Andrei B, Chris Keijdener, João M de Oliveira Barbosa, Andrei V Metrikine, and Karel N van Dalen (2021). "Transition radiation in a nonlinear and infinite one-dimensional structure: a comparison of solution methods". In: *Nonlinear Dynamics* 103.2, pp. 1365–1391.

Fărăgău, Andrei B, Traian Mazilu, Andrei V Metrikine, Tao Lu, and Karel N van Dalen (2021). "Transition radiation in an infinite one-dimensional structure interacting with a moving oscillator—the Green's function method". In: *Journal of Sound and Vibration* 492, p. 115804.

Fărăgău, Andrei B, Andrei V Metrikine, and Karel N van Dalen (2019). "Transition radiation in a piecewise-linear and infinite one-dimensional structure–a Laplace transform method". In: *Nonlinear Dynamics* 98.4, pp. 2435–2461.

Fărăgău, Andrei B, João M de Oliveira Barbosa, Andrei V Metrikine, and Karel N van Dalen (2022). "Dynamic amplification in a periodic structure with a transition zone subject to a moving load: Three different phenomena". In: *Mathematics and Mechanics of Solids*, p. 10812865221094318.

Frahm, Hermann (Apr. 1911). *Device for damping vibrations of bodies.* US Patent 989,958.

Ginzburg, VL and IM Frank (1945). "Radiation of a uniformly moving electron due to its transition from one medium into another". In: *Journal of Physics (USSR)* 9, pp. 353–362.

Hadi, Muhammad NS and Yoyong Arfiadi (1998). "Optimum design of absorber for MDOF structures". In: URL: https://doi.org/10.1061/(ASCE)0733-9445(1998)124:11(1272).

Heydari-Noghabi, H, JN Varandas, MORTEZA Esmaeili, and J Zakeri (2017). "Investigating the influence of auxiliary rails on dynamic behavior of railway transition zone by a 3D train-track interaction model". In: *Latin American Journal of Solids and Structures* 14, pp. 2000–2018.

Heydari-Noghabi, H, JA Zakeri, M Esmaeili, and JN Varandas (2018). "Field study using additional rails and an approach slab as a transition zone from slab

track to the ballasted track". In: *Proceedings of the Institution of Mechanical Engineers, Part F: Journal of Rail and Rapid Transit* 232.4, pp. 970–978.

Horníček, L, P Tyc, M Lidmila, H Krejčiříková, P Jasanskỳ, and P Břešt?'ovskỳ (2010). "An investigation of the effect of under-ballast reinforcing geogrids in laboratory and operating conditions". In: *Proceedings of the Institution of Mechanical Engineers, Part F: Journal of Rail and Rapid Transit* 224.4, pp. 269–277.

Indraratna, Buddhima, Muhammad Babar Sajjad, Trung Ngo, Antonio Gomes Correia, and Richard Kelly (2019). "Improved performance of ballasted tracks at transition zones: A review of experimental and modelling approaches". In: *Transportation Geotechnics* 21, p. 100260.

Insa, Ricardo, Pablo Salvador, Javier Inarejos, and Luis Medina (2014). "Analysis of the performance of under-sleeper pads in high-speed line transition zones". In: *Proceedings of the Institution of Civil Engineers-Transport*. Vol. 167. 2. Thomas Telford Ltd, pp. 63–77.

Insa, Ricardo, Pablo Salvador, Javier Inarejos, and Alejandro Roda (2012). "Analysis of the influence of under sleeper pads on the railway vehicle/track dynamic interaction in transition zones". In: *Proceedings of the Institution of Mechanical Engineers, Part F: Journal of Rail and Rapid Transit* 226.4, pp. 409–420.

Jin, Jie, Hyungjun Kim, Hyo-In Koh, and Junhong Park (2022). "Railway noise reduction by periodic tuned particle impact damper with bounce and pitch-coupled vibration modes". In: *Composite Structures* 284, p. 115230.

Jin, Jie, Wonseok Yang, Hyo-In Koh, and Junhong Park (2020). "Development of tuned particle impact damper for reduction of transient railway vibrations". In: *Applied Acoustics* 169, p. 107487.

Johansson, Anders, Jens CO Nielsen, Rikard Bolmsvik, Anders Karlström, and Roger Lundén (2008). "Under sleeper pads—Influence on dynamic train–track interaction". In: *Wear* 265.9-10, pp. 1479–1487.

Kaveh, A, S Mohammadi, O Khadem Hosseini, A Keyhani, and VR Kalatjari (2015). "Optimum parameters of tuned mass dampers for seismic applications using charged system search". In: *Iranian Journal of Science and Technology. Transactions of Civil Engineering* 39.C1, p. 21.

Kaveh, A and Siamak Talatahari (2010). "A novel heuristic optimization method: charged system search". In: *Acta mechanica* 213.3, pp. 267–289.

Kennedy, Justin, Peter Keith Woodward, Gabriela Medero, and Meysam Banimahd (2013). "Reducing railway track settlement using three-dimensional polyurethane polymer reinforcement of the ballast". In: *Construction and Building Materials* 44, pp. 615–625.

Kochenderfer, M.J. and T.A. Wheeler (2019). *Algorithms for Optimization*. MIT Press. ISBN: 9780262039420. URL: https://books.google.nl/books?id=uBSMDwAAQBAJ.

Kreyszig, E. (2010). *Advanced Engineering Mathematics*. John Wiley & Sons. ISBN: 9780470458365. URL: https://books.google.nl/books?id=UnN8DpXI74EC.

Krylov, V.V. (2001). *Noise and Vibration from High-speed Trains*. Knovel Library. Thomas Telford. ISBN: 9780727729637. URL: https://books.google.nl/books?id=2By9AgZYFLAC.

Kuchak, Alireza Jahan Tigh, Dragan Marinkovic, and Manfred Zehn (2021). "Parametric investigation of a rail damper design based on a lab-scaled model". In: *Journal of Vibration Engineering & Technologies* 9.1, pp. 51–60.

Li, Wei, Anbin Wang, Xiaogang Gao, Longhua Ju, and Lang Liu (2021). "Development of multi-band tuned rail damper for rail vibration control". In: *Applied Acoustics* 184, p. 108370.

Li, ZG and TX Wu (2008). "Vehicle/track impact due to passing the transition between a floating slab and ballasted track". In: *Noise and Vibration Mitigation for Rail Transportation Systems*. Springer, pp. 94–100.

Lin, CC, Jer-Fu Wang, and BL Chen (2005). "Train-induced vibration control of high-speed railway bridges equipped with multiple tuned mass dampers". In: *Journal of Bridge Engineering* 10.4, pp. 398–414.

Mottahed, Jaber, Jabbar Ali Zakeri, and Saeed Mohammadzadeh (2019). "A field investigation on the effects of using USPs in transition zone from ballasted track to bridges". In: *International journal of civil engineering* 17.9, pp. 1421–1431.

NAMURA, Akira, Yukihiro KOHATA, and Seiichi MIURA (2004). "Effect of sleeper size on ballasted track settlement". In: *Quarterly Report of RTRI* 45.3, pp. 156–161.

Nicks, Jennifer Elizabeth (2009). "The bump at the end of the railway bridge". PhD thesis. College Station, Texas, USA: Texas A & M University.

Paixão, André, Cristina Alves Ribeiro, Nuno Pinto, Eduardo Fortunato, and Rui Calçada (2015). "On the use of under sleeper pads in transition zones at railway underpasses: experimental field testing". In: *Structure and Infrastructure Engineering* 11.2, pp. 112–128.

Paixão, André, Eduardo Fortunato, and Rui Calçada (2014). "Transition zones to railway bridges: track measurements and numerical modelling". In: *Engineering structures* 80, pp. 435–443.

Read, David and Dingqing Li (2006). "Design of track transitions". In: *TCRP research results digest* 79.

Rodrigues, André Filipe da Silva (2017). "Viability and Applicability of Simplified Models for the Dynamic Analysis of Ballasted Railway Tracks". PhD thesis.

Lisbon, Portugal: Universidade NOVA de Lisboa. URL: http://hdl.handle.net/10362/21663.

Sadri, Mehran, Tao Lu, and Michaël Steenbergen (2019). "Railway track degradation: The contribution of a spatially variant support stiffness-Local variation". In: *Journal of Sound and Vibration* 455, pp. 203–220.

Al-Salami, Nada MA (2009). "Evolutionary algorithm definition". In: *American J. of Engineering and Applied Sciences* 2.4, pp. 789–795.

Sañudo, R, L Dell'Olio, JA Casado, IA Carrascal, and S Diego (2016). "Track transitions in railways: A review". In: *Construction and Building Materials* 112, pp. 140–157.

Sasaoka, Charity D and D Davis (2005). "Implementing track transition solutions for heavy axle load service". In: *Proceedings, AREMA 2005 Annual Conference, Chicago, IL*. Citeseer.

Schneider, P, Rikard Bolmsvik, and Jens CO Nielsen (2011). "In situ performance of a ballasted railway track with under sleeper pads". In: *Proceedings of the Institution of Mechanical Engineers, Part F: Journal of Rail and Rapid Transit* 225.3, pp. 299–309.

Seara, Ivo and A Gomes Correia (2010). "Performance assesment solutions for transition zones embankment-bridge railways trough numerical simulation 3D". In: *Semana de Engenharia* 2010, pp. 11–15.

Shahraki, Mojtaba, Chanaka Warnakulasooriya, and Karl Josef Witt (2015). "Numerical study of transition zone between ballasted and ballastless railway track". In: *Transportation Geotechnics* 3, pp. 58–67.

Shamalta, M and AV Metrikine (2003). "Analytical study of the dynamic response of an embedded railway track to a moving load". In: *Archive of Applied Mechanics* 73.1, pp. 131–146.

Shan, Yao, Bettina Albers, and Stavros A Savidis (2013). "Influence of different transition zones on the dynamic response of track–subgrade systems". In: *Computers and Geotechnics* 48, pp. 21–28.

Stark, Timothy D and Stephen T Wilk (2016). "Root cause of differential movement at bridge transition zones". In: *Proceedings of the Institution of Mechanical Engineers, Part F: Journal of Rail and Rapid Transit* 230.4, pp. 1257–1269.

Van Dalen, Karel N, Apostolos Tsouvalas, Andrei V Metrikine, and Jeroen S Hoving (2015). "Transition radiation excited by a surface load that moves over the interface of two elastic layers". In: *International Journal of Solids and Structures* 73, pp. 99–112.

Varandas, JN, André Paixão, and Eduardo Fortunato (2017). "A study on the dynamic train-track interaction over cut-fill transitions on buried culverts". In: *Computers & Structures* 189, pp. 49–61.

Varandas, José N, Paul Hölscher, and Manuel AG Silva (2011). "Dynamic behaviour of railway tracks on transitions zones". In: *Computers & structures* 89.13-14, pp. 1468–1479.

Vesnitskii, AI and AV Metrikin (1992). "Transition radiation in one-dimensional elastic systems". In: *Journal of applied mechanics and technical physics* 33.2, pp. 202–207.

Wang, Haoyu and Valeri Markine (2018). "Corrective countermeasure for track transition zones in railways: Adjustable fastener". In: *Engineering Structures* 169, pp. 1–14.

Wolfert, Arie Rogier Maria (1999). "Wave-Effects in One-Dimensional Elastic Systems Interacting with Moving Objects". PhD thesis. Delft, The Netherlands: Delft University of Technology. URL: http://resolver.tudelft.nl/uuid: 32cb2d0d-0660-4356-b286-18ecc4c947ed.

Wu, TX (2008). "Theoretical study on noise reduction of rail component by use of rail absorber". In: *Noise and Vibration Mitigation for Rail Transportation Systems*. Springer, pp. 384–391.

Xiao, Xin-biao, Ya-guang Li, Ting-sheng Zhong, and Xiao-zhen Sheng (2017). "Theoretical investigation into the effect of rail vibration dampers on the dynamical behaviour of a high-speed railway track". In: *Journal of Zhejiang University-SCIENCE A* 18.8, pp. 631–647.

Yang, Fan, Ramin Sedaghati, and Ebrahim Esmailzadeh (2022). "Vibration suppression of structures using tuned mass damper technology: A state-of-the-art review". In: *Journal of Vibration and Control* 28.7-8, pp. 812–836.